Tephra glass chemistry provides storage and discharge details of five magma reservoirs which fed the 75 ka Youngest Toba Tuff eruption, northern Sumatra

Pearce, Nick; Westgate, John A.; Gualda, Guilherme A. R.; Gatti, Emma; Muhammad, Ros F.

Published in:
Journal of Quaternary Science

DOI:
10.1002/jqs.3149

Publication date:
2019

Citation for published version (APA):
Pearce, N., Westgate, J. A., Gualda, G. A. R., Gatti, E., & Muhammad, R. F. (2019). Tephra glass chemistry provides storage and discharge details of five magma reservoirs which fed the 75 ka Youngest Toba Tuff eruption, northern Sumatra. *Journal of Quaternary Science*, *35*(1-2), 256-271. https://doi.org/10.1002/jqs.3149

Tephra glass chemistry provides storage and discharge details of five magma reservoirs which fed the 75 ka Youngest Toba Tuff eruption, northern Sumatra.

Nicholas J.G. Pearce[1,*], John A. Westgate[2], Guilherme A.R. Gualda[3], Emma Gatti[4], Ros F. Muhammad[5]

1. Department of Geography & Earth Sciences, Aberystwyth University, Wales, UK
2. Department of Earth Sciences, University of Toronto, ON, Canada
3. Department of Earth & Environmental Sciences, Vanderbilt University, TN, USA
4. Department of Geology and Planetary Sciences, California Institute of Technology, CA, USA
5. Department of Geology, University of Malaya, Kuala Lumpur, Malaysia

*Corresponding author: nick.pearce@aber.ac.uk

Abstract.

The Youngest Toba Tuff contains five distinct glass populations, identified from Ba, Sr and Y compositions, termed PI (lowest Ba) – PV (highest Ba), representing five compositionally distinct pre-eruptive magma batches that fed the eruption. The PI-PV compositions display systematic changes, with higher FeO, CaO, MgO, TiO_2 and lower incompatible element concentrations in the low-SiO_2 PIV/PV, than the high-SiO_2 PI-PIII compositions. Glass shard abundances indicate PV/PIV were the least voluminous magma batches, and PI/PIII the most voluminous. Pressure estimates using rhyolite-MELTS indicate PV magma equilibrated at ~6 km, and PI magma at ~3.8 km. Glass population proportions in distal tephra and proximal (caldera-wall) material describe an eruption which commenced by emptying the deepest PIV/PV reservoirs, this being preferentially deposited in a narrow band across southern India (jet-stream and/or plinian eruption transport?), and as abundant pumice-clasts low in proximal ignimbrites. Later, shallower magma reservoirs erupted, with PI being the most abundant as the eruption ended, sourcing the majority of distal ash from co-ignimbrite clouds (PI/PIII-dominant), where associated ignimbrites isolated earlier (PIV/PV-rich) deposits. This study shows how analysis of tephra glass compositional data can yield pre-eruption magma volume estimates, and enable aspects of magma storage conditions and eruption dynamics to be described.

Keywords

Youngest Toba Tuff, magma storage, glass shard chemistry, geobarometry, rhyolite, tephrochronology

Introduction

The Toba Caldera Complex of northern Sumatra, the largest Quaternary caldera on Earth, has generated three voluminous and compositionally similar rhyolitic tuffs, viz. the Oldest, Middle and Youngest Toba Tuffs, respectively dated at ~800 ka (OTT), ~500 ka (MTT) and 75 ka (YTT) by various studies (Ninkovich et al., 1978; Chesner and Rose, 1991; Chesner et al., 1991; Dehn et al., 1991; Chesner, 1998; Chesner, 2012; Storey et al., 2012; Mark et al., 2013a; Mark et al., 2013b; Mark et al., 2014; Mark et al., 2017). These tephra deposits, particularly from the YTT eruption, are widespread across Indonesia, Malaysia, India, South China Sea, Sea of Bengal, and Indian Ocean providing useful stratigraphic markers in oceanic and terrestrial environments. This is particularly true of the YTT across peninsular India, although there has been much debate about the dating of this deposit and its characterisation/identification in archaeological settings, as well as its possible impact on climate and human evolution (Rose and Chesner, 1987; Acharyya and Basu, 1993; Shane et al., 1995; Ambrose, 1998; Pattan et al., 1999; Rampino and Ambrose, 2000; Pattan et al., 2001; Oppenheimer, 2002; Chen et al., 2004; Lee et al., 2004; Pattan et al., 2010; Gatti et al., 2011; Oppenheimer, 2011; Westaway et al., 2011; Gatti, 2012; Gatti and Oppenheimer, 2012; Petraglia et al., 2012; Williams, 2012; Lane et al., 2013; Roberts et al., 2013; Costa et al., 2014; Neudorf et al., 2014). Assigning distal Toba tephra to a particular eruption using glass shard major element compositional data has proved difficult because OTT, MTT and YTT have almost identical compositions (Westgate et al., 1998; Smith et al., 2011; Gatti et al., 2014). Nonetheless, some have suggested that major element discrimination is possible, for example, using FeO (Westaway et al., 2011), but this has subsequently been discounted (Gatti et al., 2014; Pearce et al., 2014; Westgate and Pearce, 2017). Biotite major element composition provides a means to distinguish these eruptions (Smith et al., 2011), and biotite is often found in distal deposits, where small flakes travel easily within the eruption cloud. The clearest distinction of the main Toba eruptions comes from a comparison of glass trace element chemistry, although this was not recognised in early studies when only relatively small numbers of glass or single grain analyses (~20 per sample) were performed (Chesner, 1998; Chesner and Luhr, 2010; Smith et al., 2011; Matthews et al., 2012). However, the accumulation of a substantial dataset of ~3400 laser ablation (LA) ICP-MS analyses of single glass shards from proximal and distal Toba deposits by some of the current authors led (i) to the recognition of differences in the trace element compositions of OTT, MTT, and YTT and (ii) defined several characteristic glass compositional populations within YTT and MTT, but only a single population in OTT. Both of these observations are useful in defining, correlating and discriminating the various Toba deposits and, for example, have excluded the presence of OTT in any known tephra occurrences in India (Westgate et al., 2013; Pearce et al., 2014; Westgate et al., 2014; Westgate and Pearce, 2017), and ruled out the presence of Toba tephra in similar aged sequences on Flores (Brumm et al., 2016).

Here, the compositional differentiation between YTT, MTT and OTT is reviewed, and then the variation in composition within YTT tephra glass is used to describe the coexistence of multiple glass populations (and thus magma compositions) at the time of eruption. Analyses of the distribution of these glass populations allow inferences to be made about the architecture of the YTT magmatic

system, and suggest aspects of the eruption process. Detailed petrogenesis of magmas within the Toba system or YTT are not considered, and will be discussed elsewhere.

Samples and analytical methods

Data from the analysis of many distal Toba tephra samples (Westgate et al., 2013; Pearce et al., 2014; Westgate et al., 2014; Westgate and Pearce, 2017) and new analyses from a set of reconnaissance samples of proximal material have been compiled for this study. Figure 1 shows the distribution of reported Toba tephra occurrences, with named sites being those analysed for this or previous studies by the authors. The map excludes the two most distal reported YTT occurrences, Lake Malawi, East Africa (Lane et al., 2013) and the southern coast of South Africa (Smith et al., 2018).

Data were acquired from individual glass shards, or glass from pumice fragments, predominantly from the Youngest Toba Tuff, with glass shards OTT and MTT. The large number of analyses required data acquisition over many sessions, which all included reference glasses to assess accuracy and precision, and these data are presented in Supplementary Table 1. Electron probe microanalyses (EPMA) were performed at the Department of Earth Sciences, University of Toronto, using a wavelength-dispersive Cameca SX50 (15 keV accelerating voltage, 6 nA beam current, 10 µm defocused beam) calibrated from mineral and glass standards. The Lipari rhyolitic obsidian, UA5831, was used to evaluate the calibration. All analyses are normalized to 100 wt% anhydrous and total iron calculated as FeO (FeOt).

Trace element analyses were performed by laser ablation (LA)-ICP-MS in the Department of Geography and Earth Sciences, Aberystwyth University, using a Coherent GeoLas ArF 193 nm Excimer LA system coupled to a Thermo Finnegan Element 2 sector field ICP-MS. Most shards allowed analyses to be performed using 20 µm ablation craters, but some, particularly more distal material and some pumice clasts, were analysed from a mixture of 20 µm and 10 µm ablation craters. Laser fluence was 10 J cm^{-2} with a repetition rate of 5 Hz, and acquisition was 24 seconds. The internal standard was ^{29}Si, using the SiO_2 concentration determined by EPMA, after normalization to an anhydrous basis, for those shards with electron microprobe analyses. For those shards analysed only by LA-ICP-MS, 77.2 wt% SiO_2 was used as the internal standard concentration. Trace element calibration was against the NIST612 reference glass (Pearce et al., 1997) with element fractionation related to matrix differences between the reference glass and the sample being corrected (Pearce et al., 2011). The MPI-DING reference glass ATHO-G (Jochum et al., 2006; Jochum and Stoll, 2008) was routinely analysed as an unknown, and indicates analytical precision typically ±2-10%, and accuracy around ±2-5% against the published composition (GeoReM, 2014). LA-ICP-MS operating conditions are presented in more detail elsewhere (Westgate et al., 2013; Pearce, 2014; Pearce et al., 2014; Westgate and Pearce, 2017). Pumice clasts were initially crushed to separate coarser glass for analysis, however the presence of more than one glass compositional population within some pumices suggested the possible incorporation of matrix glass (i) during sample

preparation, (ii) by ballistic injection during eruption, or (iii) by mixing or mingling of magma compositions. Where all analyses from a crushed pumice clast belonged to a single glass population, these data were retained, but where more than one glass population was present, individual (whole) pumice fragments were re-prepared, with only contiguous glass being analysed. All glass analyses were inspected to remove those which showed contamination from the ablation of phenocrystic material (e.g. elevated CaO and Sr from plagioclase, or Zr and HREE from zircon) following Pearce (2014).

Distinguishing between OTT, MTT and YTT

It is not possible to distinguish unequivocally between YTT, OTT or MTT using just major element glass shard chemistry, but they can be separated using glass trace element compositions, biotite compositions or spontaneous fission track density (Smith et al., 2011; Westgate et al., 2013; Pearce et al., 2014; Westgate et al., 2014; Westgate and Pearce, 2017).

Figure 2 shows single shard analytical data from YTT, MTT and OTT to illustrate the major element similarities and trace element differences between these deposits. SiO_2 *vs* Al_2O_3 (Figure 2A) shows how all three compositions overlap, with no discernible differences. All other oxide pairs behave similarly, although minor differences in the range of some elements (e.g. CaO, Figure 2B) are apparent, there are insufficient to discriminate individual eruptions. All three of these tephra beds were derived from high-silica rhyolite magmas. These evolved towards the "granite minimum" composition (Figure 2C) with similar normative compositions (YTT – 35.6% Q', 20.9% Or', 43.5% Ab'; MTT – 35.8% Q', 22.0% Or', 42.2% Ab'; OTT – 36.0% Q', 21.3% Or', 42.8% Ab') when projected into the granite system using the method of Blundy and Cashman (2001). These magmas thus equilibrated in similar conditions, with an assemblage including high-silica rhyolitic melt, quartz and two feldspars at pressures between ~100 to 200 MPa, i.e. shallow crustal depths of <7 km (Tuttle and Bowen, 1958; Hamilton and MacKenzie, 1965; Blundy and Cashman, 2001; Gualda and Ghiorso, 2013b).

Glass trace element compositions however clearly separate YTT, MTT and OTT (Figures 2D and 2E), and while there are significant overlaps, the *range* and *distribution* of glass compositions within an eruption clearly identifies each unit: a single shard may not have a uniquely identifiable composition, but several to tens of shards will define fields which are characteristic. (Westgate et al., 2013; Pearce et al., 2014; Westgate and Pearce, 2017): In terms of Ba *vs* Y, OTT has a single low-Ba population, rarely exceeding 300 ppm, and while both MTT and YTT also contain glass shards with low Ba contents, their compositions extend to >1500 ppm Ba. When Ba and Sr concentrations are plotted against many other incompatible elements (e.g. Rb, Cs, Nb, Ta, Zr, Hf, U, Th, REE), MTT and YTT consist of several glass shard populations (Westgate et al., 2013; Pearce et al., 2014; Westgate and Pearce, 2017). These are distinct within individual eruptions, but show some overlap between eruptions (e.g. Figure 2D, where YTT glass compositions cluster at ~100 ppm, ~400 ppm, and ~700 ppm Ba, which sandwich MTT glass populations at ~250 ppm and ~450 ppm Ba). In addition to Ba-Y

or Sr-Y to define individual Toba eruptive units, some element ratios can be effective discriminators (Figure 2E), including ratios of U/LREE and Th/Nb, while many other incompatible element ratios do not distinguish the units (e.g. Zr/Nb, Hf/Ta, Nb/Y, Zr/Y).

The present-day YTT caldera encompasses the MTT caldera (now destroyed) at the north end of the modern caldera, and much of the OTT caldera to the south (Chesner, 1998; Chesner, 2012). The differences in selected trace element ratios between OTT and MTT may reflect subtle differences in the composition of magma sources, and their subsequent evolution, and the YTT eruption, with its broader composition, may have incorporated magma from earlier (and newer?) sources. Whatever the exact source and disposition of magmas feeding the main Toba eruptions, there has been a long-lived magma source, generating melts of a similar composition episodically over the last ~800 ka, and leading to the assembly of eruptible volumes of melt every few hundred thousand years. Below, the discrimination of five glass populations in YTT is discussed, and the glass population data from proximal and distal tephra deposits is considered in relation to the storage and eruption of YTT magma.

Defining five glass populations within YTT

Compiling ~700 glass trace element analyses, Westgate et al. (2013) showed for the first time that compositional clusters/gaps existed within YTT which had not been previously recognised, and defined four separate glass populations (PI-PIV) using Ba/Y, Sr/Y and Ba concentrations (see Table 2 in Westgate et al., 2013). Whilst earlier bulk sample analyses had been performed on proximal (whole-rock or glass separates) and distal samples (tephra glass concentrates), these frequently included phenocrysts, pumice fragments, lithic contaminants etc, which obfuscate the glass variation, presenting instead either a broad continuum of compositions related to large-scale magmatic evolution, or similarities in “bulk tephra” (Shane et al., 1995; Chesner, 1998; Westgate et al., 1998; Pattan et al., 2002). In early trace element studies of single-shards or glass (e.g. melt inclusions), where only ~25 analyses per sample were performed, these were too few to display the compositional groupings (Chesner and Luhr, 2010; Smith et al., 2011; Matthews et al., 2012), despite ~25 analyses being considered appropriate (Pearce et al., 2004; Pearce et al., 2007). Once several individual glass populations had been recognised, trace element analyses of other Toba tephras included, where possible, 60 to 100 shards per sample, to allow better definition of the population distributions. With 830 analyses of YTT glass available to Pearce et al. (2014) from additional analyses of some Indian samples, a small glass population between PIII and PIV of Westgate et al. (2013) was recognised, defined at the time as PIVa, with the remainder of PIV renamed PIVb. Acquisition and analysis of further YTT samples continued, adding data from the Indian Ocean and Malaysia, with further analyses of selected samples from India and analyses of proximal materials (matrix glass and pumice clasts) from Sumatra, to provide >2500 trace element analyses available for this study. Of these, 443 grains of glass have both major and trace element analyses.

Figure 3 shows Ba *vs* Y, Sr *vs* Y and Ba *vs* Sr for all single grain analyses of YTT. The data separate into five individual glass populations, which are clear in Ba *vs* Y and Sr *vs* Y, with three populations evident at lower concentrations of Ba *vs* Sr. The adjacent histograms (Ba/Y, Sr/Y and Ba/Sr) show minima in the abundance of analyses which reflect some of the compositional gaps in the bivariate plots. For this larger dataset, it is clear that the simple ratio or concentration criteria used by Westgate et al. (2013) to define populations are no longer appropriate, and thus here a new series of glass population definitions have been chosen (see Table 1). These are based on either (i) the minima in Ba/Y or Sr/Y ratios (the solid lines in Figure 3) or (ii) where element ratios do not bisect the gap between populations, the line separating the densest regions of data (dashed lines not intersecting the origin in Figure 3). These were used to assign each YTT glass shard to a population. Where a contradictory assignment was generated by different criteria, inspection of the data was undertaken such that (i) for PIV and PV (i.e. for higher Ba and Sr concentrations), Ba *vs* Y and Sr *vs* Y were used to assign a population, and not Ba *vs* Sr; (ii) between PIII and PIV, Ba/Y was used preferentially to Sr/Y; (iii) between PIV and PV, Sr/Y was used preferentially to Ba/Y. Inevitably, some analyses sit close to boundaries between populations, and, if distributions within each population are near normal, it is inevitable that a few grains will be assigned to a neighbouring population. In addition, the presence of ablated phenocrystic material, which may not be apparent immediately from the analyses, could also affect the assignment of a few shards. In particular high Sr associated with high CaO and lower incompatible elements is an indication of feldspar ablation, and Ba may indicate ablation of biotite or feldspar too, and Y would be added to an analysis (with Zr) from zircon or allanite (Pearce, 2014). In some cases, some of these may go unrecognised because of the extensive range of Sr and Ba shown by the glass shards from YTT. In some LA-ICP-MS analyses it is not entirely obvious whether for example the high Sr, accompanied by a near-typical CaO, relates to feldspar ablation, or to a high Sr glass grain, and where this doubt exists the analyses have been left in the dataset. Inspection of trace element data after assignment into populations suggests that these issues probably affect <1% of the >2500 analyses, some of which may well be part of the normal variation within different populations.

YTT glass population compositions and abundances.

Table 2 shows the average composition of each glass population within YTT and gives the numbers of analysed shards per population. The shard abundances per population from proximal, distal and pumice glass analyses are given in Table 3. The change from element ratios or concentrations to define populations in earlier studies (Westgate et al., 2013; Pearce et al., 2014) makes little difference to the population abundances.

Many trace elements show a steady, systematic variation between populations, not only for Ba, Sr and Y, but for almost all other elements (see Table 2). PI has the lowest Ba and Sr and PV the highest. From PI to PV concentrations of the LREE (La – Sm), and Eu increase, whilst Rb, Y, Zr, Nb, Cs, the MREE and HREE (Gd – Lu), Ta, Th, and U decrease. Average Pb and Hf remain almost constant across the five populations. Figure 4 presents a selection of compositional data, including Zr *vs* Y and

Rb *vs* Cs, illustrating some of these changes. Within an individual population some elements show constant ratios, which differ between populations. These often overlap and are generally inadequate to define populations, although PI is often almost distinct (e.g. Zr-Y, Figure 4A). In contrast, other elements (e.g. Cs-Rb, Figure 4B) show a gradual change in concentration from one population to the next, retaining a constant ratio (Cs/Rb) across all populations. Selected element ratios are presented in Table 2. The REE show a systematic change from PI, with low LREE, high HREE (and thus shallowest normalised REE pattern) and the deepest negative Eu anomaly, to PV, with the steepest REE pattern (i.e. high LREE, low HREE), and the shallowest negative Eu anomaly (see Figure 4C).

From the major element analyses of YTT glass alone, it is not possible to recognise distinct populations, although some differences are evident in reported analyses associated with post-depositional environmental variation, e.g. sea water induced leaching (Gatti et al., 2014). However, those glass shards analysed for both major and trace elements display a systematic change in major element composition when assigned to populations (see Figures 4E to 4H and Table 2). Here, almost 0.5 wt% SiO_2 separates the average compositions of PI and PV, which varies systematically across the populations (see histograms in Figure 4). PIV and PV have the lowest SiO_2 and show subtly higher FeO, CaO, MgO, TiO_2 and K_2O than PI and PII, with PIII compositionally in the middle. Additionally, the lower SiO_2 in PIV and PV is associated with generally lower incompatible element concentrations (Y, REE, Th, U) than PI-PIII, and higher Ba and Sr, indicating a systematic variation in the range of magma compositions released during the YTT eruption (see Table 2).

The division of YTT glass into five populations is based on the analysis of proximal and distal material from 30 widely spaced sites across Sumatra, Malaysia, the Indian Ocean and peninsular India. This includes distal ash fall glass (1554 analyses), and from proximal ignimbrites matrix glass (165 shards) and individual pumice lapilli glass (778 analyses). It seems probable that this array of analyses gives a first approximation of the relative volumes of magma which were erupted, as it covers a range of materials and environments. Indeed considering only distal or proximal glass analyses (see Table 3) it is apparent that there are significant differences in abundance between these regions (presumably related to eruption processes and modes of deposition, see below). Whilst the proximal sampling is relatively limited (8 sites), it can be assumed that all analyses combined closely approximate the proportions of erupted magma types. Taking the dense rock equivalent (DRE) volume of the YTT eruption as 5300 km^3, comprising 3800 km^3 DRE of tephra fall deposits and 1500 km^3 of proximal ignimbrite (Costa et al., 2014), the volume of each magma composition can be calculated from glass population proportions (GPP) (see Table 3). Even the "smaller" glass populations (PII, PIV and PV) then represent ~500 km^3 DRE of magma, an order of magnitude more than the ejecta from Crater Lake, Oregon, or the Santorini caldera. The more abundant PI and PIII (~2000 km^3 DRE) compare with the largest described Quaternary super-eruptions from Yellowstone or Taupo Volcanic Zone.

Magma storage conditions from YTT glass populations

The YTT glass compositions record equilibration of high-silica rhyolite melt with quartz, plagioclase, sanidine, and a fluid phase, which can be used to yield information on magmatic equilibration conditions (Tuttle and Bowen, 1958; Blundy and Cashman, 2001; Gualda and Ghiorso, 2013b; Gualda and Ghiorso, 2014). Experimental studies of the haplogranite system show that the position of the quartz-feldspar cotectic varies with pressure, moving towards more silica-rich compositions at lower pressures (Tuttle and Bowen, 1958); thus, granitic melts in equilibrium with quartz and feldspar are more silicic at lower pressure (shallower crustal levels). Plotting the position of granitic melts onto the water saturated Q'-Ab'-Or' system (see Figure 2) thus can determine equilibration pressures (Tuttle and Bowen, 1958; Luth et al., 1964; Hamilton and MacKenzie, 1965; Blundy and Cashman, 2001). This relationship links variations in SiO_2 concentrations with pressure (Gualda and Ghiorso, 2013b) whereby the SiO_2 content provides a geobarometer for quartz and feldspar saturated silicic magmas in middle to upper crustal settings (Gualda and Ghiorso, 2013). However, errors associated with a graphical approach may be of ~0.35 wt% SiO_2 for a given pressure, which almost covers the compositional range of the five YTT glass populations. Better is a numerical approach, which can give a more accurate estimate of the pressure of equilibration between rhyolitic magmas (represented by glass in tephra deposits) and quartz and feldspar. This is achieved by calculation of the quartz and feldspar saturation surfaces as a function of pressure using rhyolite-MELTS (Gualda et al., 2012), which reveals the pressure at which each glass composition may have equilibrated with quartz, sanidine, and plagioclase (as observed in the natural samples). The pressure obtained is that at which the melt last equilibrated with the observed crystal assemblage; for pyroclastic rocks this is an excellent proxy for the pressure of crystallization in the pre-eruptive magma body (Bégué et al., 2014; Gualda and Ghiorso, 2014; Pamukcu et al., 2015).

Using the average major element composition for each YTT glass population, equilibration pressures (with quartz and two feldspars) were calculated using rhyolite-MELTS for water saturated conditions, with oxygen fugacity at the Ni-NiO (NNO) buffer (appropriate for granite magmas), and these are presented in Table 4. Calculated equilibration pressures range from 102 MPa for PI to 158 MPa for PV, with a steady decrease in pressure with increasing SiO_2 content (cf. Gualda and Ghiorso, 2013b). These pressures equate to depths of magma storage between ~3.8 km (PI) to ~6 km (PV) assuming an average crustal density of 2.7 g cm^{-3} (see Table 4). The range in SiO_2 concentrations for each population (1 s.d. ranging between 0.23 to 0.29 wt%) is approximately the same as that derived solely from analytical variation from homogeneous media, for example ATHO-G 75.46±0.31 wt% (1 s.d., n=91) (Westgate et al., 2019). However, the compositional trends evident in the major element data (e.g. increasing SiO_2 with decreasing Na_2O+K_2O, see Figure 4H) suggest the variation within each population represents both a combination of EPMA analytical precision and real SiO_2 variation associated with magmatic evolution within each population. Thus to estimate the potential depth range over which each magma batch may have been stored, the relationship between calculated depth and SiO_2 content has been applied to the average ± 1 standard deviation SiO_2 content for each population (see Figure 5 and Table 4). This suggests the individual magma bodies may have had a

thickness of around 2 – 2.5 km. This is greater than the magnitude of errors in calculated pressure estimates for rhyolite-MELTS, which are typically ~20 MPa (~0.75 km), which generally derive from analytical uncertainties related to alkali mobility in glass, minimised here by optimising EPMA conditions (Kuehn et al., 2011; Westgate et al., 2013; Pearce et al., 2014; Westgate and Pearce, 2017). The calculated depths of YTT magma storage coincide with the seismically near-isotropic zone below the caldera at depths less than ~7 km, this being the region that can be assumed to have been affected and disrupted by the YTT eruption (Jaxybulatov et al., 2014). Additionally, these pressure estimates conform to others derived from H_2O and CO_2 gas saturation from melt inclusions in quartz of 100-140 MPa (Chesner and Luhr, 2010) and from experimental studies which suggest magmas resided at between 100-150 MPa immediately prior to eruption (Gardner et al., 2002).

Zircon saturation temperatures (T_{ZS}) have been calculated following Watson and Harrison (1983) – WH83 – and Boehnke et al., (2013) – B13 – for each of the YTT glass populations (see Table 4). Resulting temperature ranges for PI-PV are 766-782 °C (WH83) or 719-736 °C (B13). In general, temperatures based on the calibration of Watson and Harrison (1983) agree better with independent geothermometers (see Pamukcu et al., 2015). These T_{ZS} represent the final equilibration between melt and zircon, under zircon-saturated conditions; as such, they likely represent the pre-eruptive conditions just prior to eruption, similar to the pressures calculated using the rhyolite-MELTS geobarometer. Temperatures calculated here are 40-50 °C higher than the lowest T_{ZS} calculated from matrix- or melt-inclusion glass by Reid and Vasquez (2017) of 726-757 °C (WH83) or 670-706 °C (B13) using compositional data from Chesner (1998) and Chesner and Luhr (2010). The cause for the discrepancy is unknown. In general, the temperatures obtained are consistent with those observed for other high-silica rhyolite magmas equilibrated at shallow crustal levels (e.g. Gualda and Ghiorso, 2013a; Bégué et al., 2014; Pamukcu et al., 2015). Our results suggest small (<15 °C) differences in temperature between the various glass populations – PIV and PV show the highest temperatures, while PI-PIII show slightly lower temperatures. This is consistent with the idea that the different compositional groups represent distinct magma batches, each one characterized by its own storage conditions.

Spatial distribution of glass population proportions (GPP) within YTT

Figures 6 and 7 show the glass population proportions (GPP) of PI-PV in samples of YTT, including shards from distal tephra deposits, and matrix shards (eight sites) or individual pumice fragments (seven sites) from proximal ignimbrites near to/within the YTT caldera. GPP are presented as pie charts from each site, which vary in the number of analyses (see Supplementary Table 2). Selected "average" glass compositions are illustrated for comparison. In some cases, a few samples from the same site or region have been pooled to represent the lower abundance populations accurately. Reworking of distal deposits in fluvial systems (e.g. Malaysia, India) will average the regional deposition (Gatti, 2012; Gatti and Oppenheimer, 2012) and justifies grouping local deposits. For the various deposit types GPP are summarised in Table 3, with GPP for all samples given in Supplementary Table 2.

Distal glass shards: Figure 6 shows the GPP within distal tephra, but this shows no strikingly obvious, broad-scale geographical variation. Nonetheless, subtle but significant variations in GPP do exist. Overall, the distal tephras contain much less PV glass than proximal deposits (both matrix glass and pumice, see Table 3, *cf*. Figure 7). Across northern and eastern India, PIII glass is abundant (~50%) whereas in Malaysia and the eastern Bay of Bengal, PI is the most abundant population (~50%), and PIV and PV are lowest. PV is generally low abundance to the north of the equator with the exception of a series of samples which run in a rough line northwest from the Toba caldera across peninsular India, including Kurnool (the most abundant occurrence of distal PV, at 23% of 70 analyses, and the lowest PI at 11%), as well as relatively high amounts of PIV and PV at Morgaon, Bori, and from the marine core sample SO138-269 KL in the northern Arabian Sea (see Figure 1 for locations). The sample from Jawalapuram resembles the sites in NE India, with low PV. Two sites ~3000 km southwest of the Toba caldera in the Central Indian Ocean Basin (CIOB) (ABPII/90 and ABPII/111) also have higher than average PV glass (from 40-80 analyses per sample). The core SO93-51KL intercepted a 20 cm thick deposit of YTT, from which three sub-samples were analysed (see Figure 6 and Supplementary Table 2), which shows very low PIV and PV throughout, and a 20% increase in PI towards the top of the layer, concomitant with a decrease in PII and PIII. Marine tephra deposition can be complicated by rafting and subsequent density current sinking (Carey, 1997), which may affect the compositional profile recorded in thick ash layers; nonetheless, the SO93-51KL core does show some vertical variation.

Proximal glass shards: Figure 7 shows GPP for free matrix shards and pumice clasts from proximal deposits near the Toba caldera. Samples containing pumice were collected from different elevations above the base of the YTT ignimbrite, i.e. near Muara (at ~20 m above YTT base), above Haranggaol (40 m and 130 m above base), Siguragura (~55 m), and near Sipisupisu (~65 m). Samples from Ajibatar (950 m ASL), Lontung (at 1433 m ASL), and the matrix-only samples UT1298 (Bakara), UT2319 (east-central shore of Lake Toba) and UT2320 (Balige) are all from unknown elevations above the YTT base. Whilst modest in number, these samples provide a first look at glass and pumice compositional variation with location and stratigraphic height above the base of YTT. This approach, as described below, has potential to elucidate some of the eruptive history.

The GPP of proximal matrix glass (165 analyses, 8 samples) is dominated by PI, with >60% in all but two samples (Figure 7, Table 3). Matrix glass samples from Muara (~20 m above base), and Balige however are dominated by PV glass, with no PI glass, and occur in the southeastern caldera walls where limited PIV proximal matrix glass occurs (5 shards only). The proximal GPP thus differ markedly from distal shards, containing around three times more PV and ~50% more PI glass, and less than half the PII, PIII and PIV glass. The lower Haranggaol sample (H1270m) contains some PII matrix glass (also Sipisupisu) which is not present in the younger Haranggaol (H1360m) sample. Thus, despite modest numbers of analyses, a geographical division in GPP is evident.

Pumice clasts: As with proximal matrix glass, the GPP of individual pumice clasts also show spatial and stratigraphic variation in the ignimbrites (Figure 7). Analyses of crushed or contiguous pumice clasts show only negligible differences (see Table 3 and Supplementary Table 2), arguing against significant incorporation of matrix glass into the analysed crushed pumices. Nonetheless, in Figure 7, only contiguous or single-population crushed pumice analyses are presented.

Pumice clasts from Muara (~20 m above YTT base) are dominated by PV glass, and about 50% of the glass in pumices from H1270m (~40 m above YTT base) is PV, with both sites showing pure PV pumice clasts. Restriction of PV pumice to low levels indicates (i) that PV magma was erupted early and (ii) upward reworking of material was not significant, suggesting original stratigraphy is largely maintained, a situation seen in many other ignimbrites (e.g. the Tshirege Member of the Bandelier Tuff, where flow units are well stratified both compositionally and thermally, with little reworking, Westgate et al., 2019). Abundant pure PI pumices occur at H1270m, Sipisupisu and H1360m, and in the latter two localities, they are accompanied by many pure PIII pumices, suggesting the onset of the eruption of PIII magmas may have been later than for PI, PIV, and PV magma. The sole pure PIV pumice comes from Lontung (Samosir), at an unknown elevation above the YTT base, and here remaining pumices are pure PI. The only pure PII pumice comes from Siguragura, occurring with several pure PI and the only pure PIII clast. PII comprises only 4% of pumice glass. PIII pumice appears more abundant in the northern/eastern caldera walls, with several pure PIII clasts at Sipisupisu and Haranggaol, and one from Siguragura.

Most pumices containing more than 1 population are from the mingling of two compositions. Table 5 shows numbers of pumice clasts (from 40) with only one or two glass populations: pure PI, PIII and PV pumices are most abundant. Most commonly, PIV and PV, and PIII and PIV occur together indicating that these compositions interacted extensively during eruption. Two pumice clasts from Ajibata contain PIII, PIV, and PV glass. PI occurs in 16 pumice clasts, of which 14 are pure PI, with remaining two are from Haranggaol 1270 m (PI, PII, PIV, PV, 15 analyses) and Muara (PI, PII, PIII, 6 analyses). Mingling of magmas was only visible in one pumice clast (from Sipisupisu) where dark and light portions were analysed separately and contained differing proportions of PII and PIII glass (see Figure 7).

Implications for magma storage and eruption from tephra glass compositions

From the identification of five separate glass populations representing compositionally distinct magma batches within YTT, which equilibrated at different depths, and from the spatial distribution of these glass populations in both proximal and distal tephra and pumice deposits, an initial attempt can be made to synthesize these data into a model for the eruption which produced the YTT.

The presence of abundant PV pumice and matrix glass, alongside PIV matrix glass in the oldest (lowest) proximal YTT ignimbrites indicates that these compositions were plentiful in early erupted material. PIV and PV magmas equilibrated at the highest pressures (~150-160 MPa), and their early

eruption may relate to the destabilisation of the entire Toba system as one/both of these reservoirs gradually became primed and started to erupt, or that the eruption process was initiated by the arrival of hot magma from depth (Bachmann et al., 2014; Wolff et al., 2015; Bachmann and Huber, 2016; Tramontano et al., 2017). The frequent mingling of PIV and PV in pumices (see Table 5), and their compositional association (Figures 4 and 5), may indicate a physical proximity or connection between the two magma batches, and mingling with PIII may also indicate interaction between these magma bodies on eruption. In contrast, the marked compositional separation of PI from PII (Figures 4 and 5), and paucity of mingled PI pumice clasts (see Table 5), might suggest that PI magma existed both chemically and physically separate from the other magma compositions.

PV glass is also unusually abundant in tephra deposits between Kurnool and Bori (India) and from core SO93-289KL (Arabian Sea), and these also contain elevated quantities of PIV glass, whereas abundances of PIV and PV glass are low NE and SW of this band. This early erupted material must have been transported as a fairly tightly constrained plume, NW from the Toba caldera, possibly within high level easterly (summer) jet-stream winds (cf. Valles caldera deposits, Westgate et al., 2019), consistent with a suggested northern hemisphere summer eruption (Schulz et al., 1998; Bühring and Sarnthein, 2000). The early erupted PIV/PV material may have been either an early plinian phase to the eruption, or elutriated material forming a co-ignimbrite plume, transported by prevailing tropospheric or stratospheric winds (Schulz et al., 1998; Schott and McCreary Jr, 2001). Two samples from the Central Indian Ocean Basin (~10 °S), ~ 3000 km from the caldera also contain elevated PIV/PV and low PI, again suggesting an association with the early part of the eruption. Transport to produce these more southerly deposits may have been either from co-ignimbrite ash, or the migration of a plinian eruption plume, but is unlikely to be related to migration of equatorial jets so far south (Schott and McCreary Jr, 2001).

PIV and PV are absent from pumice from the higher stratigraphic levels (H1360m and Siguragura), indicating that PI, PII and PIII magmas, released from shallow to intermediate depth reservoirs, dominated the later erupted material. Across India, PIII glass is most abundant in areas away from those where the PIV/PV glass is abundant. These PIII-rich deposits (containing little or no PV) are likely to be derived from co-ignimbrite plumes associated with eruption of the large-volume PI and PIII magma bodies, with lesser amounts of PII, and the continuing eruption of small volumes of PIV magma. Ignimbrites associated with the eruption of large, shallow magma reservoirs would have buried and isolated any early erupted PV glass. As the eruption proceeded, the upwards increase in the PI:PIII ratio within the YTT deposit from SO93-51KL suggest either the eruption of PIII magma declined, or PI increased, with PI, the most voluminous composition, continuing to be ejected until late in the eruption. This may reflect generally decreasing intensity/mass eruption rates later in the eruption, with more PI-rich co-ignimbrite ash deposited closer to Sumatra, eastern Bay of Bengal and the Malaysian peninsula. Because of the complexity of the atmospheric circulation in this region (Bühring and Sarnthein, 2000; Schott and McCreary Jr, 2001), and order of magnitude variations in estimates of YTT mass eruption rates and duration (Woods and Wohletz, 1991; Costa et al., 2014), detailed modelling of ash dispersal has not been attempted here.

The draining of the sub-caldera magma reservoirs thus appears to have commenced with eruption of the smaller and deepest magma bodies (PV and PIV), and proceeded to the eruption of larger and shallower bodies (PIII, PII and PI) until the end of activity. The abundances of mixed population pumice clasts suggests that PIII, PIV and PV were closely connected during eruption, but that PI erupted with limited interaction with other magma reservoirs. This also appears to reflect the chemical "proximity" of individual populations. Nonetheless, relatively early in the eruption limited mingling of all magma reservoirs occurred (giving a few pumices with 3 or 4 populations of glass, Table 5). The YTT eruption must thus have occurred from several vents and linear or ring-fracture segments across the present caldera (Knight et al., 1986; Chesner and Rose, 1991; Chesner, 1998; Chesner, 2012), involving both vertical and lateral magma movement (Gravley et al., 2007; Cashman and Giordano, 2014; Kennedy et al., 2018a; Kennedy et al., 2018b).

Combining equilibration pressures, GPP (to give relative magma volumes) and compositional features of all three major Toba eruptions, a cartoon of the magmatic system below the YTT caldera shortly before eruption can be generated (Figure 8). The illustrated vertical extent of each magma body is based on the depths calculated from their SiO_2 contents, with areas being proportional to their volumes based on a 5800 km^3 eruption (Costa et al., 2014). The difference between OTT and MTT in U/Ce and Th/Nb suggests possible differences in source compositions for these magmas, and a broadly similar variation is seen in U/Ce for glass from YTT, with PIV and PV having the lowest ratios, similar to MTT, and PI the highest, similar to OTT. Combined with variations in other elements (e.g. Ba, Sr, Rb) and ratios (e.g. Zr/Y) these factors may suggest that PIV and PV magmas were sourced/accumulated under the NW of the current caldera (and can be loosely regarded as more MTT type), with PI accumulating in the SE, underlying the OTT caldera and similar to OTT magma compositions in many respects (low Ba, high U/Ce). PIII may be a mixture of both low and high U/Ce and Th/Nb sources.

The abundant PIII magma (29.6%), an intermediary composition in terms of U/Ce and Ba (~750 ppm Ba), is not observed in MTT or OTT deposits, appearing first during the YTT eruption. PIII may thus be either a mixture of new magma batches from earlier OTT and MTT sources, or remelting of crystal mushes in the sub-caldera complex associated with intrusion of basic material at depth (Bachmann et al., 2014; Wolff et al., 2015; Bachmann and Huber, 2016; Reid and Vazquez, 2017), to generate a composition intermediate between PI and PV. Magma production/accumulation under the Toba caldera has clearly continued post-YTT eruption, as evidenced by post caldera lava domes., and the dramatic uplift of Samosir Island in the last 30 ka (Chesner, 2012; Mucek et al., 2017). Geophysical studies suggest a large magma body exists to ~10 km depth under the southern two thirds of the caldera (Samosir and south), with a smaller body to the north (Masturyono et al., 2001). More recently a sub-crustal/lower crustal basic magma reservoir feeding upwards into a radially seismically anisotropic layered sill complex, extending to depths of about 7 km, has been suggested, immediately underlying a seismic low velocity zone that was potentially disturbed by the YTT eruption (Koulakov et al., 2009; Jaxybulatov et al., 2014; Koulakov et al., 2016). The various depths

for magma storage proposed in these studies and the structure and disposition of magma bodies are consistent with the pressure estimates of magma equilibration from the tephra glass compositions.

Conclusions

The YTT eruption at 75 ka erupted five discrete magma compositions (PI-PV), identified by glass shard Ba, Sr and Y contents from tephra deposits. This aspect of the YTT eruption had not been recognised in bulk analysis of proximal deposits. Major element compositions of YTT glass shards show systematic variation associated with equilibration at different depths. The low volume, high-Ba PV magma equilibrated at ~ 6 km, and the low-Ba, largest volume PI magma equilibrated at ~3.8 km, depths similar to magma storage in other large caldera systems e.g. Yellowstone (Swallow et al., 2018); Taupo Volcanic Zone (Bégué et al., 2014; Gualda et al., 2019); Bishop Tuff (Wallace et al., 1999; Gualda and Ghiorso, 2013a); Peach Spring Tuff (Pamukcu et al., 2015); among many others. The YTT eruption commenced by emptying the deepest magma reservoirs, perhaps as a plinian eruption, with abundant PV magma (±PIV) being carried in a relatively narrow plume across parts of India, as well as proximal ignimbrite deposition at lower stratigraphic levels.

The eruption proceeded to expel magma from higher crustal levels, initially PIII, as deeper reservoirs gradually emptied, with PI becoming most abundant towards the end of the eruption. During later stages of the eruption, distal tephra was deposited from co-ignimbrite clouds. The presence of multiple magma reservoirs under large calderas is widely recognised from studies in the proximal realm (Gravley et al., 2007; Cooper et al., 2012; Gualda and Ghiorso, 2013b; Bégué et al., 2014; Alloway et al., 2015; Cooper et al., 2016; Swallow et al., 2018), and is evident in the YTT glass compositional data from both proximal ignimbrites and distal tephra fall deposits. Here, the abundance and distribution of individual glass populations in both distal and proximal YTT deposits provides details of magma equilibration conditions, and clearly links tephrochronology to the petrogenesis of the magmas, the evolution of the eruption, and the possible distribution processes of tephra. This approach offers a roadmap to link tephra analyses and stratigraphy to magma chemistry and petrogenesis, and to storage and eruption dynamics, thereby extending the scope of tephrochronological studies.

Acknowledgements

Funds provided by the Natural Sciences and Engineering Research Council of Canada to JAW are gratefully acknowledged. Field studies to enable the collection of proximal material were funded by grants to RFM from the Malaysian Ministry of Higher Education (FP079-2007) and Malaysian Ministry of Science, Technology and Innovation (04-01-03-SF0301). Work by GARG was partly funded by the US National Science Foundation (EAR-1151337). We are grateful to Craig Chesner, Ravi Korisettar, Martin Williams and Sacha Jones who kindly provided samples of YTT from India and Malaysia to JAW for analysis, to Hermann Kudrass for providing samples from the Sonne-93 (SO93) cruise to EG, and Jinnappa Pattan and Shyam Prasad, NIO Goa for samples from the CIOB. NJGP

would like to thank Paul Asimov and Paula Antoshechkina at California Institute of Technology for their time and help introducing him to rhyolite-MELTS. This paper contributed to “The interplay of physical volcanology, tephrochronology, and petrology in understanding volcanoes” session at the INTAV meeting in Brasov, Romania, June/July 2018. Thanks are due to the handling editor, Britta Jensen, and the referees for their comments on an earlier draft of this paper.

TABLES

Table 1. Ratios or linear divisions between clusters of compositions used to discriminate between the five glass populations observed within YTT, based on Ba *vs* Y, Sr *vs* Y, and Ba *vs* Sr. Ba *vs* Y and Sr *vs* Y are used to identify PI-PV, with Ba *vs* Sr also used for PI – PIII. Italicised ratio values in parenthesis indicate the minima in Sr/Y or Ba/Y from the histograms in Figure 3, used previously to separate populations (Westgate et al., 2013; Pearce et al., 2014). Element concentrations in ppm.

YTT pop'n boundary	**Ba *vs* Y**	**Sr *vs* Y**	**Ba *vs* Sr**
PI-PII	Ba = 4.5 Y	Sr = 0.8 Y	Ba = 2.817 Sr + 126.8
PII-PIII	Ba = 6.375 Y + 122.5 *(ratio min. Ba/Y = 10)*	Sr = 1.039 Y + 14.225 *(ratio min. Sr/Y = 1.35)*	Ba = 3.636 Sr + 265.5
PIII-PIV	Ba = 13 Y + 290 *(ratio min. Ba/Y = 22)*	Sr = 1.538 Y + 19.23 *(ratio min. Sr/Y = 2)*	Ba = 6.633 Sr + 280
PIV-PV	Ba = 27 Y	Sr = 2.091 Y + 16.182 *(ratio min. Sr/Y = 2.55)*	Not used

Table 2. Average major and trace element composition of individual glass populations (I-V) within YTT (assigned according to criteria in Table 1), and the overall YTT average. Major elements normalised to an anhydrous basis with H_2O_d the average water content calculated by difference from the original analytical total. "n" is the number of glass analyses within each population, and for major element populations this is where both EPMA and LA-ICP-MS were performed on the same grain. "All" is the average of all major or trace element analyses on glass shards, and for major elements includes those grains (104 analyses) with **no** trace element analyses.

Glass pop'n	**I**		**II**		**III**		**IV**		**V**		**All**	
Major elements, wt %												
n=	**192**	**s.d.**	**56**	**s.d.**	**87**	**s.d.**	**15**	**s.d.**	**77**	**s.d.**	**531**	**s.d.**
SiO_2	77.376	0.281	77.314	0.264	77.175	0.287	76.969	0.279	76.914	0.226	**77.229**	**0.312**
TiO_2	0.087	0.056	0.102	0.057	0.074	0.051	0.091	0.086	0.097	0.088	**0.089**	**0.061**
Al_2O_3	12.555	0.147	12.607	0.152	12.622	0.133	12.723	0.134	12.729	0.134	**12.606**	**0.155**
FeO_t	0.854	0.058	0.867	0.057	0.891	0.053	0.911	0.073	0.913	0.095	**0.881**	**0.070**
MnO	0.086	0.047	0.070	0.032	0.082	0.039	0.064	0.030	0.072	0.039	**0.079**	**0.042**
MgO	0.047	0.020	0.056	0.021	0.061	0.022	0.057	0.022	0.080	0.028	**0.057**	**0.025**
CaO	0.682	0.055	0.741	0.049	0.787	0.070	0.823	0.066	0.897	0.072	**0.756**	**0.098**
Na_2O	3.166	0.182	3.112	0.175	3.106	0.166	3.089	0.104	3.104	0.117	**3.159**	**0.179**
K_2O	5.030	0.155	5.027	0.210	5.103	0.195	5.174	0.206	5.109	0.152	**5.040**	**0.185**
Cl	0.152	0.046	0.136	0.046	0.129	0.043	0.128	0.045	0.111	0.038	**0.136**	**0.046**
-O=F,Cl	-0.034		-0.031		-0.029		-0.029		-0.025		**-0.031**	
H_2O_d	3.380	1.468	3.811	1.652	3.757	1.459	3.882	1.264	3.105	0.656	**3.670**	**1.391**
Total	100.000		100.000		100.000		100.000		100.000		**100.000**	
Trace elements, ppm												
n=	**954**	**s.d.**	**326**	**s.d.**	**743**	**s.d.**	**213**	**s.d.**	**262**	**s.d.**	**2507**	**s.d.**
Rb	292	31	255	23	232	28	216	27	200	31	253	45
Sr	28.9	7.4	57.2	9.1	75.4	12.6	96.2	14.7	113	18	61.0	31.3
Y	69.8	12.0	53.9	10.0	49.0	9.0	45.4	8.7	36.9	6.7	56.1	15.1
Zr	116	20	117	18	131	25	143	26	144	29	126	26
Nb	23.9	3.2	20.2	2.8	19.6	3.7	18.7	2.8	17.5	2.8	21.0	4.1
Cs	10.8	1.6	8.26	1.00	6.98	1.20	5.96	0.87	5.12	1.15	8.34	2.53
Ba	94.5	30.7	392	52	701	107	1025	137	1191	188	507	402
La	34.3	5.0	38.6	5.6	45.1	7.1	54.9	11.5	68.0	14.9	43.3	13.4
Ce	66.0	8.8	70.5	8.1	77.8	10.7	88.3	13.4	106.6	19.1	76.2	16.9
Pr	8.02	1.89	8.08	1.36	8.78	1.52	9.93	2.07	11.1	2.07	8.74	2.05
Nd	30.9	6.7	30.2	6.3	32.3	7.0	35.8	9.6	37.4	8.5	32.3	7.5
Sm	8.24	2.35	7.03	2.00	7.13	2.29	7.71	2.60	7.09	2.37	7.59	2.32
Eu	0.36	0.38	0.53	0.36	0.63	0.43	0.71	0.48	0.75	0.51	0.53	0.50
Gd	8.89	2.95	7.02	2.45	6.87	2.94	6.92	2.88	6.14	3.19	7.60	3.13
Tb	1.58	0.44	1.23	0.36	1.11	0.35	1.09	0.39	0.94	0.38	1.29	0.46
Dy	10.6	2.4	8.46	2.15	7.83	2.20	7.62	2.53	6.30	2.16	8.81	2.72
Ho	2.37	0.57	1.86	0.47	1.72	0.47	1.63	0.50	1.37	0.47	1.94	0.62
Er	7.65	1.70	5.98	1.64	5.49	1.50	5.21	1.55	4.20	1.24	6.23	1.97
Tm	1.29	0.36	0.99	0.32	0.90	0.31	0.83	0.29	0.71	0.30	1.04	0.39
Yb	8.93	2.01	6.83	1.45	6.35	1.62	5.93	1.51	4.86	1.41	7.21	2.21
Lu	1.44	0.42	1.11	0.34	1.02	0.35	0.96	0.33	0.77	0.35	1.16	0.44
Hf	6.05	1.58	5.48	1.51	5.92	1.86	5.88	1.67	5.60	1.73	5.88	1.65
Ta	3.76	0.75	2.89	0.55	2.77	0.85	2.49	0.59	2.15	0.67	3.08	0.93
Pb	60.9	15.8	62.9	16.5	59.1	21.1	58.3	19.9	57.1	17.5	60.0	18.9
Th	64.3	11.8	52.5	9.2	50.5	9.2	49.6	9.4	45.8	9.2	55.5	12.1
U	10.5	1.5	8.07	1.09	7.02	1.32	6.33	1.78	5.28	0.93	8.25	2.32
Selected trace element ratios												
Sr/Y	0.42	0.10	1.08	0.17	1.57	0.27	2.16	0.43	3.09	0.43	1.27	0.90
Ba/Y	1.36	0.40	7.41	1.02	14.6	2.4	23.0	2.9	32.7	4.1	11.2	10.5
Zr/Y	1.67	0.15	2.19	0.17	2.69	0.30	3.18	0.46	3.91	0.50	2.40	0.79
Zr/Ce	1.76	0.22	1.66	0.17	1.70	0.36	1.62	0.23	1.35	0.18	1.68	0.30
Zr/Nb	4.88	0.69	5.85	0.80	6.74	0.92	7.66	1.10	8.24	1.29	6.15	1.49
U/Ce	0.16	0.02	0.12	0.01	0.09	0.02	0.07	0.02	0.05	0.01	0.12	0.04
Ce/Th	1.04	0.13	1.36	0.14	1.57	0.24	1.81	0.26	2.36	0.31	1.44	0.46
Rb/Th	4.66	0.81	4.97	0.86	4.73	0.96	4.49	0.91	4.55	1.16	4.70	0.92
Cs/Th	0.17	0.04	0.16	0.03	0.14	0.03	0.12	0.03	0.12	0.03	0.15	0.04
Th/Nb	2.69	0.39	2.61	0.37	2.60	0.38	2.66	0.38	2.62	0.39	2.65	0.38
U/Y	0.15	0.03	0.15	0.03	0.15	0.03	0.14	0.03	0.15	0.03	0.15	0.03

Table 3: Proportions (as percentage of all analyses) of the different glass compositional populations (PI-PV) in YTT, i.e. distal glass shards (i.e. not from Sumatra), proximal matrix glass shards (from YTT ignimbrite deposits in the Toba caldera walls) and pumice (from clasts within YTT ignimbrites exposed in the caldera). Population compositions are defined using the criteria in Table 1 (see also Figure 3). * - Magma volume is calculated from the 5300 km^3 estimate for the DRE of the YTT eruption from Costa et al. (2014). In earlier studies, using the criteria in Westgate et al. (2013) the population distributions were PI - 38.7%, PII - 14.0%: PIII -37.4%: PIV - 9.8% (where their PIII has since become PIII and PIV, and their PIV is now PV). Pearce et al. (2014) population distributions would have been PI - 38.7%, PII - 14.0%: PIII -29.0%: PIVa – 8.4%: PIVb - 9.8% (where their PIVa has since become PIV, and their PIVb is now PV).

Glass pop'n	All glass analyses (shards/ pumice)	Magma volume* DRE, km^3	Glass shard analyses			Pumice clast analyses	
			All	Distal	Proximal matrix	Contiguous/ single pop Only	All (contiguous/ crushed
PI	**38.1%**	2017	**38.9%**	36.6%	60.6%	35.1%	**36.2%**
PII	**13.0%**	689	**17.2%**	18.0%	9.1%	3.6%	**3.9%**
PIII	**29.6%**	1571	**31.1%**	33.1%	12.1%	27.3%	**26.5%**
PIV	**8.5%**	450	**7.6%**	8.0%	3.0%	11.3%	**10.5%**
PV	**10.5%**	554	**4.8%**	3.7%	15.2%	22.7%	**22.8%**
Shards analysed	**2507**		**1719**	1554	165	670	**788**

Table 4. Magma storage conditions calculated for each of the five glass populations in YTT, by various methods based on aspects of the composition of the different glass populations. r-MELTS: calculations of equilibration pressures (with quartz and two feldspars) from average major element composition calculated using rhyolite-MELTS for water saturated conditions, and oxygen fugacity at the Ni-NiO (NNO) buffer(Gualda and Ghiorso, 2014). Depth calculated using an average crustal density of 2.7 g cm^{-3}. Zircon sat^{n}: Zircon saturation temperatures calculated from Zr content and aspects of the major element composition of each glass population, based on the two widely used models of zircon solubility, WH83 (Watson and Harrison, 1983) and B13 (Boehnke et al., 2013).

Glass pop'n	**SiO_2 wt% (avg ± s.d.)**	**P (MPa) (avg ± s.d.) r-MELTS**	**Depth km (avg ± s.d.) (ρ=2.7 gcm^{-3})**	**Zr ppm (avg ± s.d.)**	**Zircon sat^{n} T °C (WH83)**	**Zircon sat^{n} T °C (B13)**
PI	77.376 ± 0.281	102 ± 34	3.8 ± 1.3	116 ± 20	766	719
PII	77.314 ± 0.264	107 ± 32	4.0 ± 1.2	117 ± 18	767	720
PIII	77.175 ± 0.287	127 ± 35	4.8 ± 1.3	131 ± 25	775	729
PIV	76.969 ± 0.279	148 ± 34	5.6 ± 1.3	143 ± 26	782	737
PV	76.914 ± 0.226	158 ± 28	6.0 ± 1.0	144 ± 29	782	736

Table 5. Numbers of individual pumice clasts that show either one or two populations of glass (i.e. 40 single or dual population pumice clasts in total) are shown in the table (e.g. there are 6 pure PIII clasts, and 6 clasts containing PIV and PV glass). Only four additional pumice clasts (making the total pumice clasts analysed = 44) show more than two populations of glass and these are from; Ajibata (two clasts with PIII, PIV, PV); Haranggaol 1270 m (PI, PIII, PIV, PV); Muara (PI, PII, PIII, but from a very small sample with n=6).

Glass pop'n	**PI**	**PII**	**PIII**	**PIV**	**PV**
PI	14				
PII	0	1			
PIII	0	2	6		
PIV	0	0	4	1	
PV	0	0	1	6	5

FIGURES.

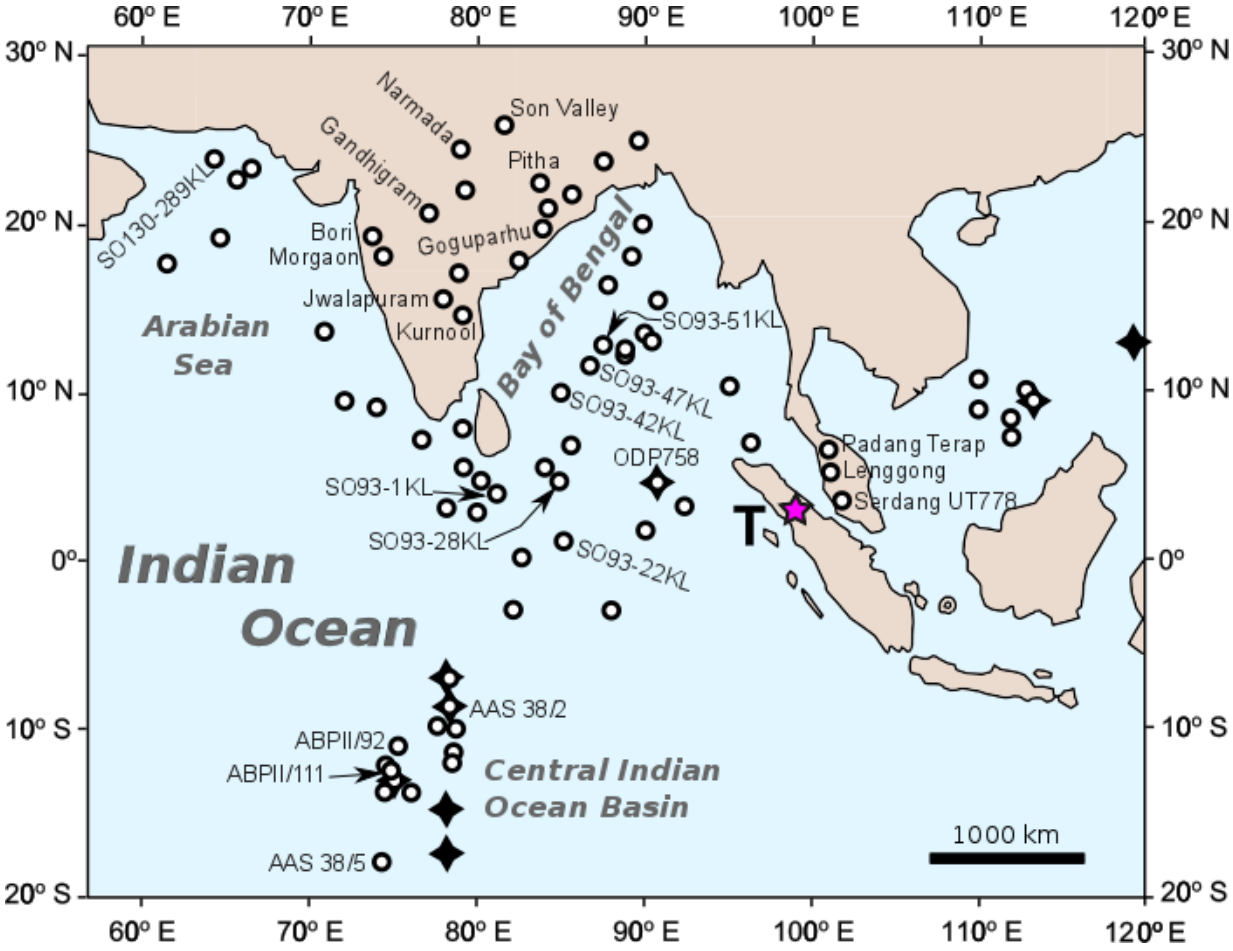

Figure 1. Distribution of Toba tephra occurrences, including those samples analysed as part of this study from named sites. O - YTT occurrences: ✦ - OTT occurrences. MTT only recorded at ODP-Site 758. Location of Toba caldera **T** ☆. Marine occurrences prefixed "SO" are from the Sonne-93 cruise (Weber et al., 2003). Map excludes YTT occurrences from Lake Malawi, East Africa (Lane et al., 2013) and on the southern coast of South Africa (Smith et al., 2018). For locality information, see Supplementary Table 2.

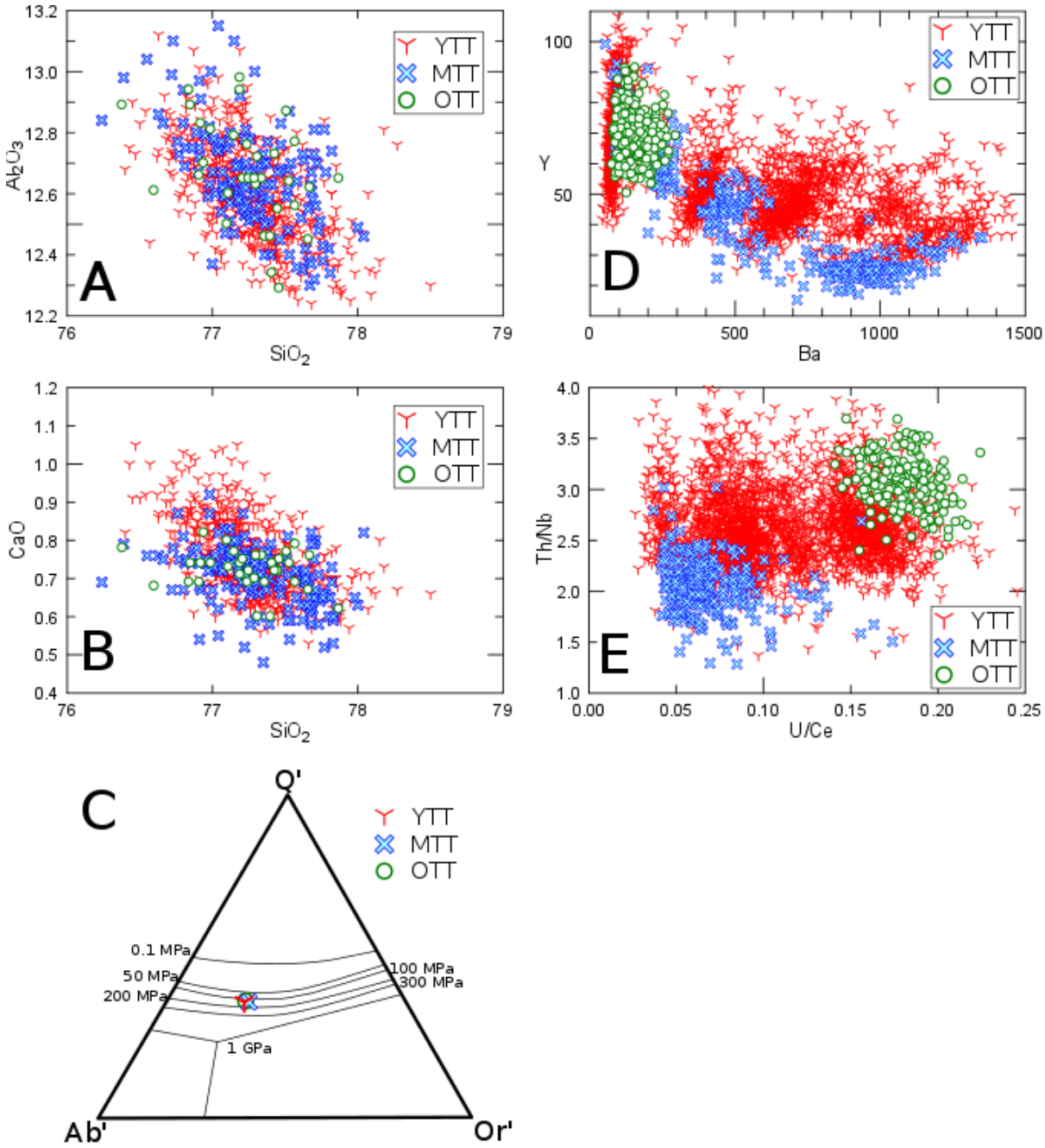

Figure 2. Selected compositional data for YTT, MTT and OTT. **A and B**: SiO_2 *vs* Al_2O_3 and SiO_2 *vs* CaO (all wt %) show the similarity in composition of the three major Toba eruptive units, although subtle differences in the range of CaO can be seen. **C:** Normative compositions plotted in the granite system following the method of Blundy and Cashman (2001) Q' – quartz, Ab' – albite, Or' – orthoclase, calculated to include the effects of An (anorthite) on equilibria in the granite system. **D:** Ba *vs* Y (ppm) shows the fields of composition occupied by YTT, MTT and OTT, which can be used to identify the three units. **E:** U/Ce *vs* Th/Nb shows a clear separation of MTT (Layer C of ODP 758 and the MTT Vitrophyre) from OTT, but YTT glass more or less encompasses the range of the other units. Similarly U/other LREE, Th, U and Rb also show good compositional separation between MTT and YTT. See text for discussion and sources.

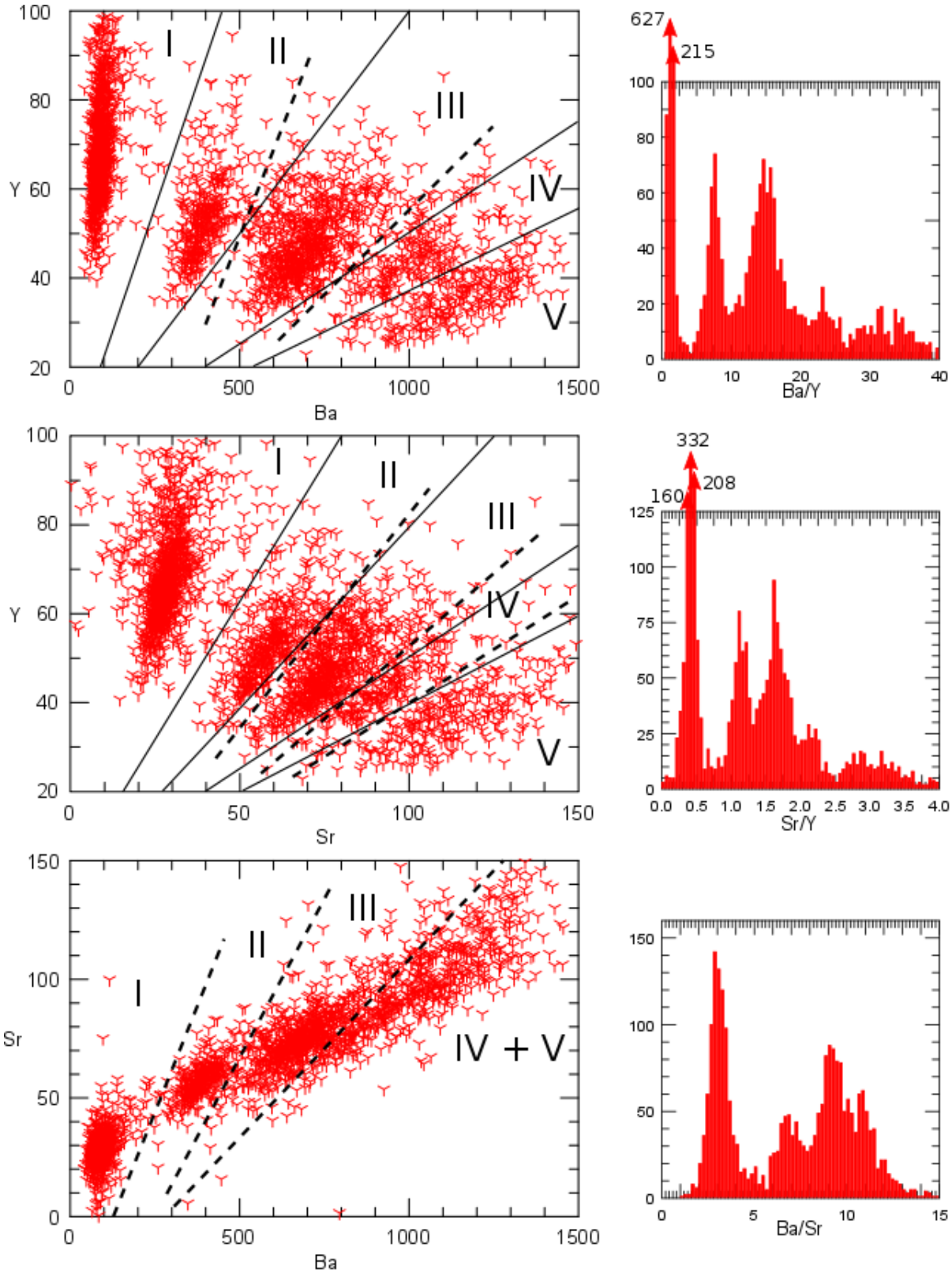

Figure 3. Bivariate plots of Ba *vs* Y, Sr *vs* Y and Ba *vs* Sr (all as ppm), and histograms of Ba/Y, Sr/Y and Ba/Sr for 2507analyses of glass from YTT performed by LA-ICP-MS, to show the criteria for separation of glass into different populations (PI – PV). The axes on the x-y diagrams have been scaled to show the clearest spread in the data – about 15 analyses exceed 1500 ppm Ba and 150 ppm Sr (and all belong to PV), and about 10 analyses exceed 100 ppm Y (all PI). On the histograms a

few ratios exceed the maximum bin value shown on the x axis, and the “Frequency” axis has been scaled to show detail for the lower frequencies. Solid lines on the Ba *vs* Y and Sr *vs* Y plots which intersect the origin are ratios taken from the minima in the Ba/Y and Sr/Y histograms, and are used to separate PI-PII and PIV-PV (Ba *vs* Y) and PI-PII (Sr *vs* Y). Dashed lines on all plots are fitted visually through the lowest density regions of data points and are used to separate the remaining populations, although the continuum in Ba *vs* Sr compositions at high Ba and Sr makes separation of PIV and PV difficult using these elements.

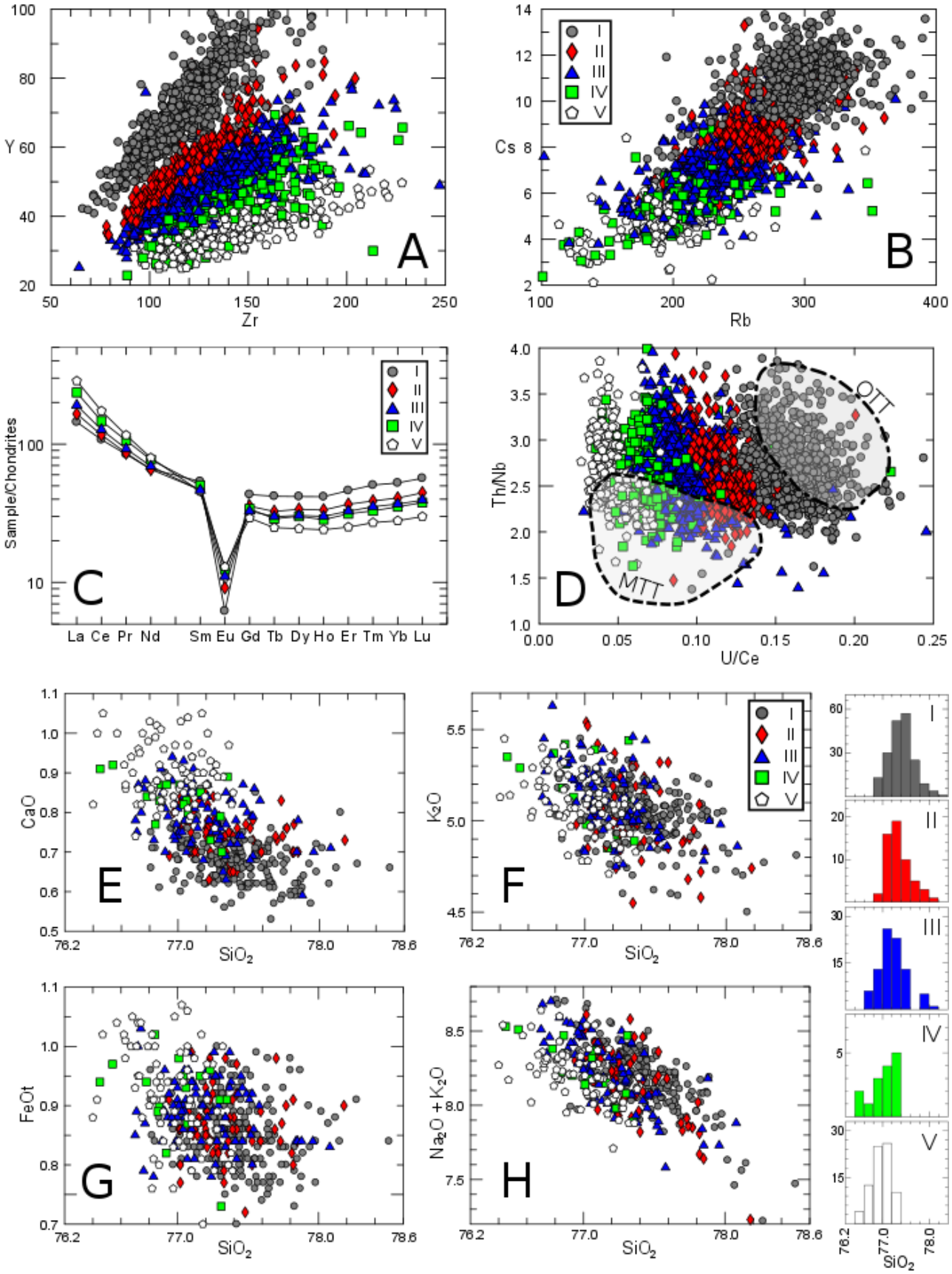

Figure 4. Selected bivariate compositional plots (trace and major element) for YTT glass shards subdivided into their separate populations. Concentrations in ppm (trace elements) and wt% (major

element oxides). **A:** Zr *vs* Y shows individual glass populations have different ratios of Zr/Y, and similar behaviour is seen for many other HFSE element pairs including Zr/LREE, Zr/U, Zr/Nb, Zr/Th, U/Ce (U/LREE), LREE/Nb, and LREE/Th. **B:** Rb *vs* Cs show a near-constant element ratio across all populations, although the average compositions of each population vary systematically (*cf*. Table 2). Similar behaviour is seen for many other incompatible element pairs including Rb/Th, Cs/Th, U/Cs, Th/Nb, U/Y (U/HREE) as well as from the compatible elements Sr/Ba. **C:** Chondrite normalised average REE composition of each glass population within YTT, displaying a steady and systematic change from PI to PV. Chondrite compositions from Sun and McDonough (1989). **D:** U/Ce *vs* Th/Nb for the 5 glass populations of YTT compared to MTT and OTT (see also Figure 2). **E-H:** Selected major element oxides from YTT glass shards, grouped into their respective glass populations (PI-PV) from the trace element analyses of the same shards. Note the steady decrease on CaO, K_2O, FeO and (Na_2O + K_2O) with increasing SiO_2. **Histograms** show the distribution of SiO_2 within the five glass populations, with PI having the highest SiO_2, and PV the lowest.

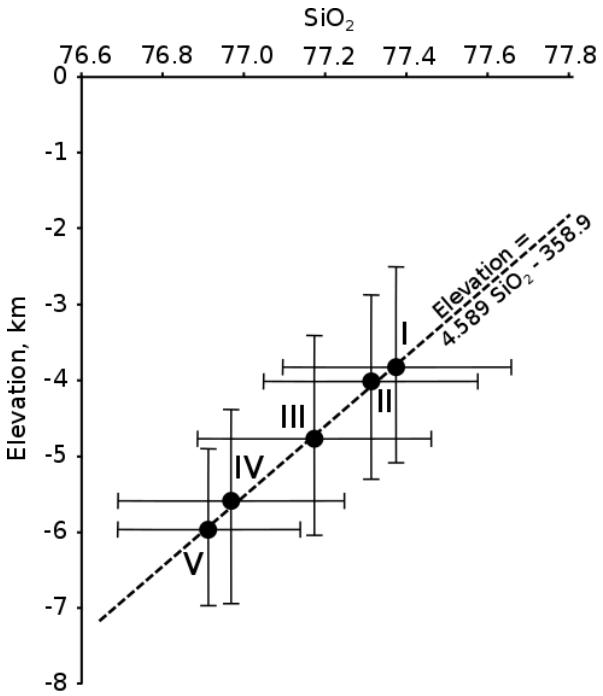

Figure 5. Relationship between the SiO_2 content (wt%) and depth of equilibration (given as Elevation in km) for each of the individual glass populations (marked I – V), calculated from the pressure modelled in rhyolite-MELTS, and converted to depth assuming crustal density is 2.7 g cm^{-3}. Horizontal error bars show ±1 standard deviation for the SiO_2 concentration of each population, which has been converted to an equivalent elevation (depth) range (vertical error bars) using the best-fit line between SiO_2 and elevation through the five average population compositions (equation given, r=0.9976).

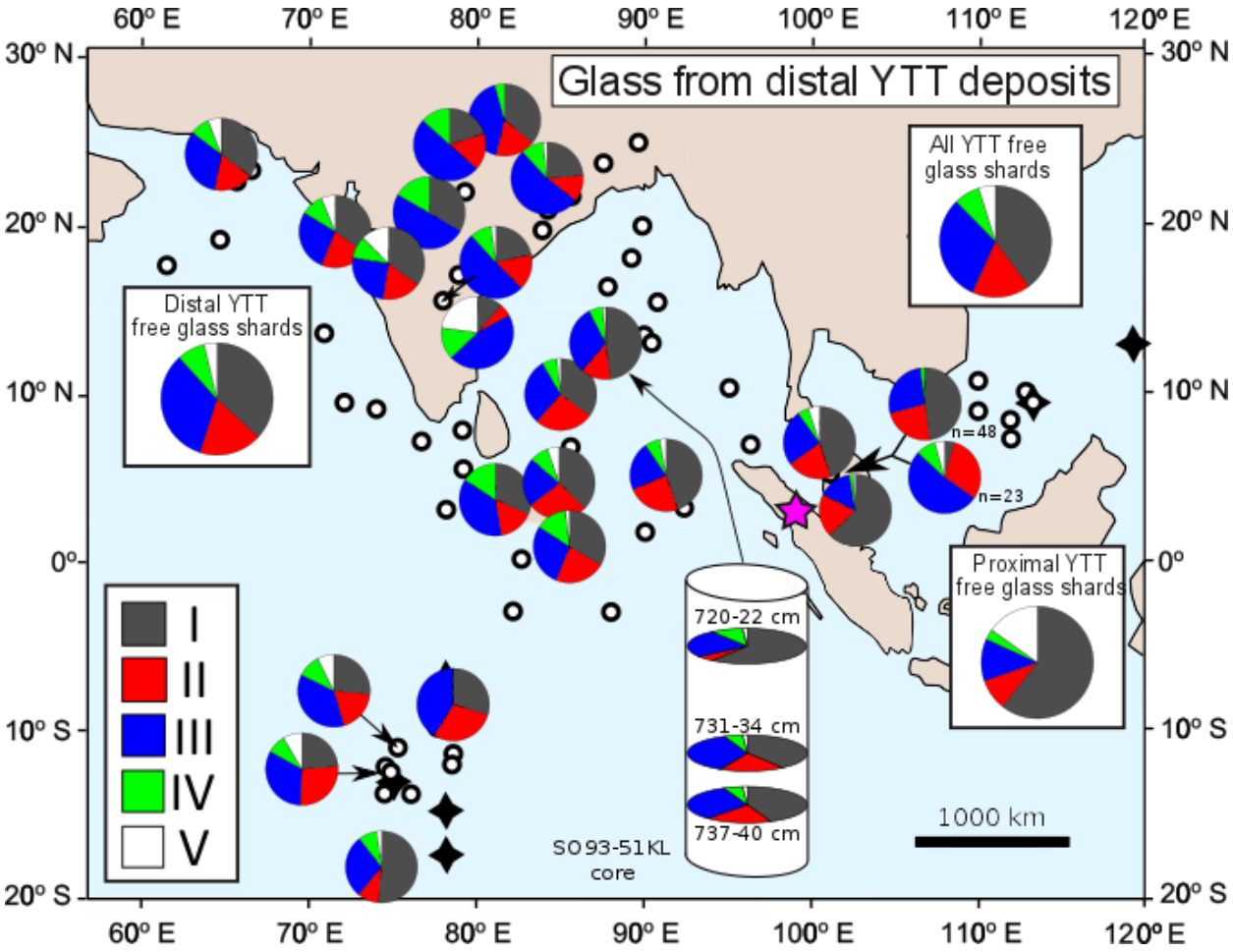

Figure 6. Glass population proportions (GPP) as pie-charts from distal YTT tephra deposits across the Indian Ocean, peninsular India and Malaysia centred (where possible) above their point of occurrence, with arrows indicating otherwise (*cf*. Figure 1). Boxed insets show the GPP all YTT free glass shard analyses, all proximal glass shards, and all distal glass shards, but not pumice glass analyses (see Figure 7). Reworking of the distal deposits in fluvial systems (e.g. Malaysia, India) will "average" the regional deposition. Inset diagram of a core shows variation in GPP from three analysed sub-samples from core SO93-51KL, which contains a 20 cm thick YTT deposit (depth ranges sampled are indicated). The average data for this core is shown on the map. This core sample is dominated by PI and PIII, however PI shows a marked increase from ~40% in the lower samples to ~60% in the upper sample, concomitant with a dramatic decrease in PII and PIII. See Supplementary Table 2 for individual sample location information, numerical shard counts and GPP.

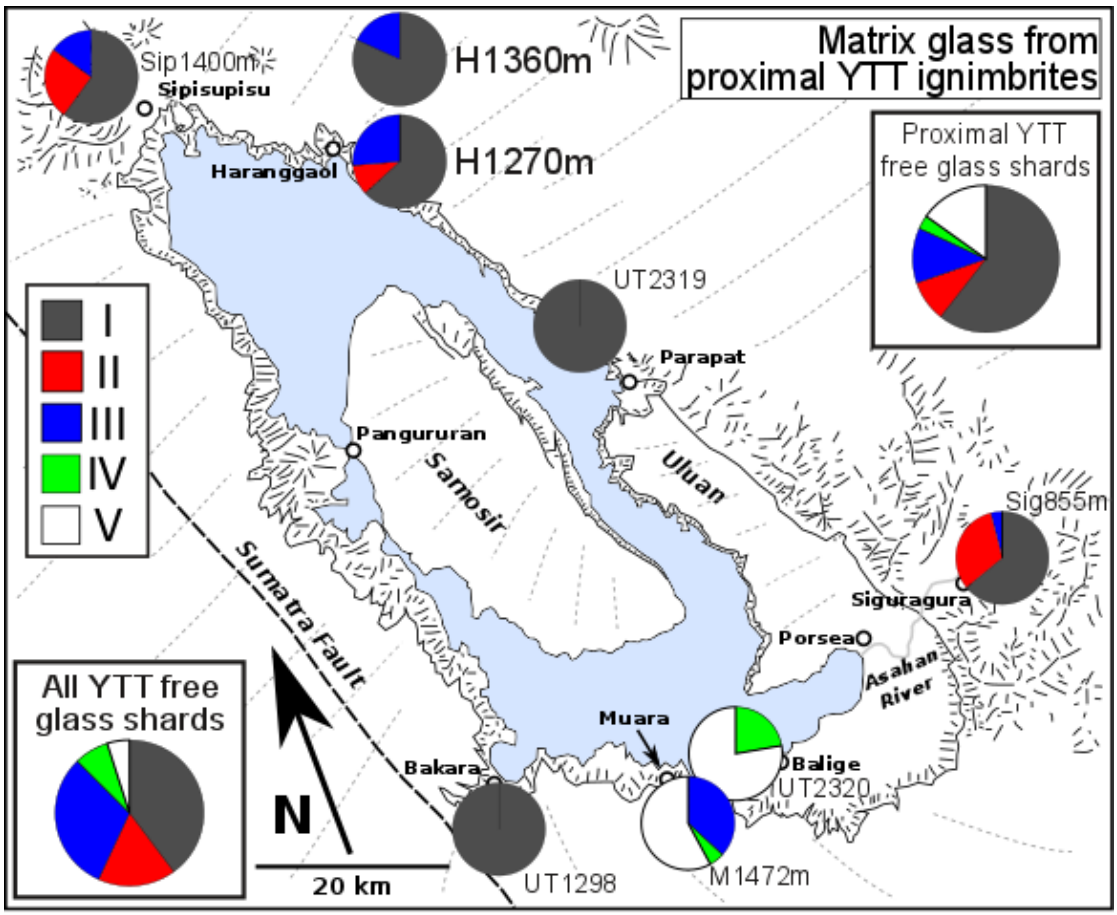
Matrix glass from proximal YTT ignimbrites
Sip1400m
Sipisupisu
H1360m
Haranggaol
H1270m
Proximal YTT free glass shards
UT2319
Parapat
Pangururan
Samosir
Uluan
Sig855m
Siguragura
Porsea
Asahan River
Sumatra Fault
I
II
III
IV
V
All YTT free glass shards
N
20 km
Muara
Balige
Bakara
UT2320
UT1298
M1472m

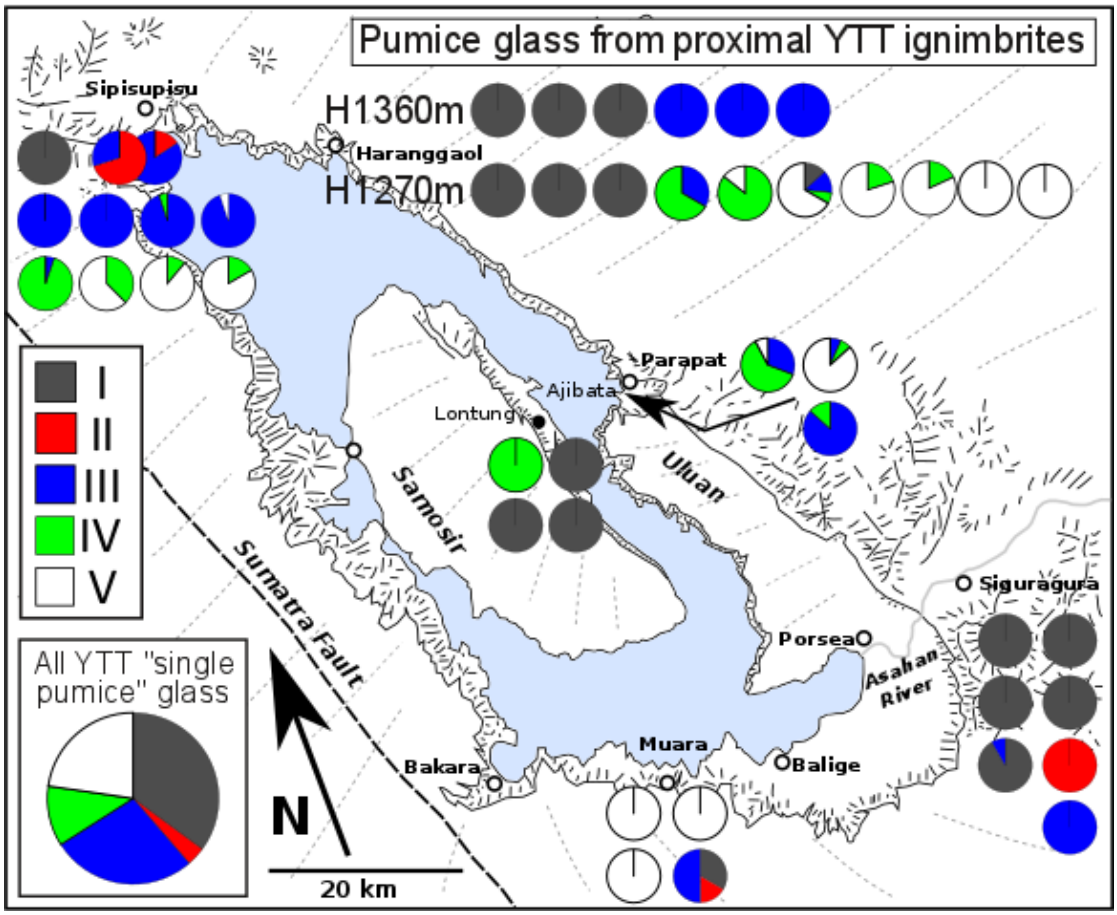
Pumice glass from proximal YTT ignimbrites
Sipisupisu
H1360m
Haranggaol
H1270m
Parapat
Ajibata
Lontung
Samosir
Uluan
Siguragura
Porsea
Asahan River
Sumatra Fault
I
II
III
IV
V
All YTT "single pumice" glass
N
20 km
Muara
Balige
Bakara

Figure 7. Proximal glass population proportions (GPP) from YTT ignimbrite samples around the Toba caldera. **Upper diagram:** Free glass shards from the sample matrix. **Lower diagram:** Glass from individual pumice clasts within the ignimbrites. Samples were collected at various distances above the base of the YTT ignimbrite, where it contacts MTT in the north and OTT in the south (Knight et al., 1986; Chesner and Rose, 1991), and within the caldera. Sample positions are listed below with ascending stratigraphic height above the local base of the YTT ignimbrites:-

H1360m Haranggaol: 130 m YTT base (1230 m), sample from 1360 m
Sipisupisu: 65 m above YTT base (1335 m), sample from 1400 m
H1270m Haranggaol: 40 m above YTT base (1230 m), sample from 1270 m
Muara: 20 m above YTT base (1450 m), sample from 1470 m

At Siguragura, the YTT base is much lower (800 m) and samples were collected from 855 m (+55 m). At Sipisupisu, the two overlapping pie charts are two sets of analyses from dark (left pie-chart) and light (right pie-chart) portions of a single pumice clast showing varying proportions of PII and PIII. See Supplementary Table 2 for individual sample location information, numerical shard counts and GPP.

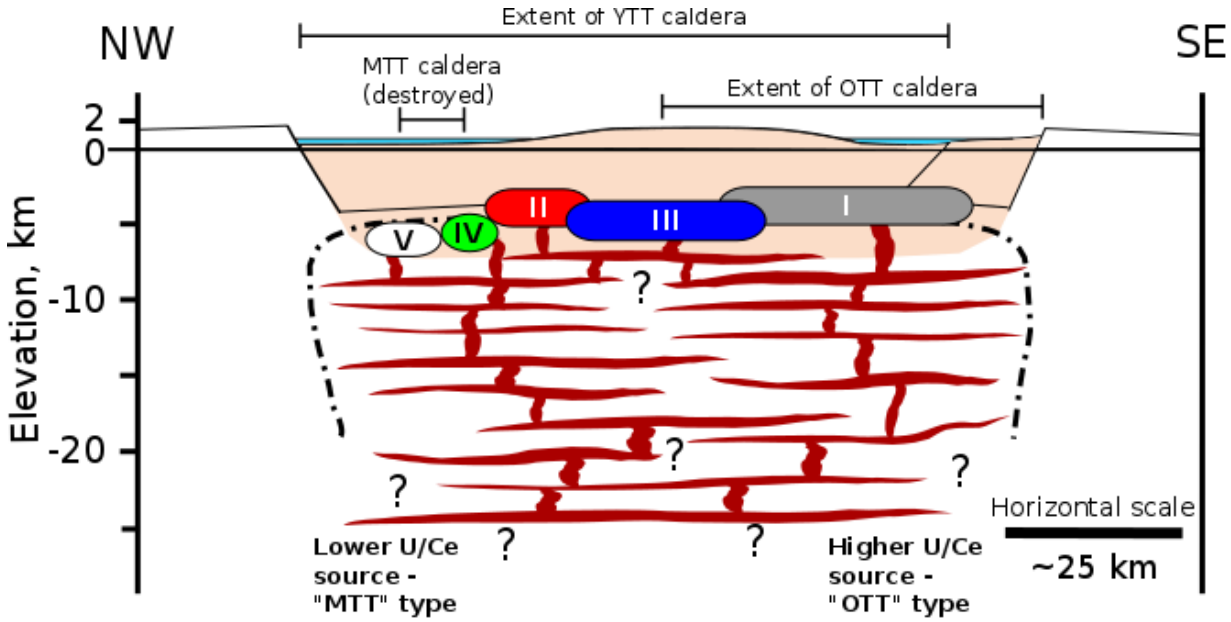

Figure 8. Cartoon cross section of the possible configuration of magma bodies under the YTT caldera at 75 ka. Note 2x vertical exaggeration. Surface topography represents roughly the present day landform, with the resurgent Samosir Island at the centre of the caldera. Magma reservoirs of the different populations are labelled I – V, and their areas are in proportion to the numbers of analyses of each glass population (see Table 3), with equilibration depths given in Table 4. The shaded area under the caldera represents material disrupted by the YTT eruption with the sub-caldera sill complex indicated below this (Jaxybulatov et al., 2014).

References

Acharyya, S.K., Basu, P.K., 1993. Toba ash on the Indian subcontinent and its implications for correlation of Late Pleistocene alluvium. Quaternary Research, 40: 10-19.

Alloway, B.V., Pearce, N.J.G., Villarosa, G., Outes, V., Moreno, P.I., 2015. Multiple melt bodies fed the AD 2011 eruption of Puyehue-Cordón Caulle, Chile. Scientific Reports, 5.

Ambrose, S.H., 1998. Late Pleistocene human population bottlenecks, volcanic winter, and differentiation of modern humans. Journal of Human Evolution, 34(6): 623-651.

Bachmann, O., Deering, C.D., Lipman, P.W., Plummer, C., 2014. Building zoned ignimbrites by recycling silicic cumulates: insight from the 1,000 km 3 Carpenter Ridge Tuff, CO. Contributions to Mineralogy and Petrology, 167(6): 1025.

Bachmann, O., Huber, C., 2016. Silicic magma reservoirs in the Earth's crust. American Mineralogist, 101(11): 2377-2404.

Bégué, F., Deering, C., Gravley, D., Kennedy, B., Chambefort, I., Gualda, G., Bachmann, O., 2014. Extraction, storage and eruption of multiple isolated magma batches in the paired Mamaku and Ohakuri eruption, Taupo Volcanic Zone, New Zealand. Journal of Petrology, 55(8): 1653-1684.

Blundy, J., Cashman, K., 2001. Ascent-driven crystallisation of dacite magmas at Mount St Helens, 1980-1986. Contributions to Mineralogy and Petrology, 140(6): 631-650.

Boehnke, P., Watson, E.B., Trail, D., Harrison, T.M., Schmitt, A.K., 2013. Zircon saturation re-revisited. Chemical Geology, 351: 324-334.

Brumm, A., Van den Bergh, G.D., Storey, M., Kurniawan, I., Setiabudi, E., Alloway, B.V., Setiawan, R., Yurnaldi, D., Moore, M.W., Puspaningrum, M., Insani, H., Sutisna, I., Meije, H.J.M., Grün, R., Westgate, J.A., Pearce, N.J.G., Duval, M., Aziz, F., Sutikna, T., van der Kaars, S., Morwood, M.J., 2016. Age and context of the oldest known hominin fossils from Flores. Nature, 534: 249-253.

Bühring, C., Sarnthein, M., 2000. Toba ash layers in the South China Sea: Evidence of contrasting wind directions during eruption ca. 74 ka. Geology, 28(3): 275-278.

Carey, S., 1997. Influence of convective sedimentation on the formation of widespread tephra fall layers in the deep sea. Geology, 25(9): 839-842.

Cashman, K.V., Giordano, G., 2014. Calderas and magma reservoirs. Journal of Volcanology and Geothermal Research, 288: 28-45.

Chen, C.-H., Lee, M.-Y., Iizuka, Y., Dehn, J., Wei, K., Carey, S.N., 2004. First Toba supereruption revival: comment and reply. Geology, 35: 54-55.

Chesner, C.A., 1998. Petrogenesis of the Toba Tuffs, Sumatra, Indonesia. Journal of Petrology, 39: 397-438.

Chesner, C.A., 2012. The Toba Caldera Complex. Quaternary International, 258: 1-18.

Chesner, C.A., Luhr, J.F., 2010. A melt inclusion study of the Toba Tuffs, Sumatra, Indonesia. Journal of Volcanology and Geothermal Research, 197(1): 259-278.

Chesner, C.A., Rose, W.I., 1991. Stratigraphy of the Toba Tuffs and evolution of the Toba Caldera Complex, Sumatra, Indonesia. Bulletin of Volcanology, 53: 343-356.

Chesner, C.A., Rose, W.I., Deino, A., Drake, R., Westgate, J.A., 1991. Eruptive history of Earth's largest Quaternary caldera (Toba, Indonesia) clarified. Geology, 19: 200-203.

Cooper, G.F., Wilson, C.J., Millet, M.-A., Baker, J.A., 2016. Generation and rejuvenation of a supervolcanic magmatic system: a case study from Mangakino volcanic centre, New Zealand. Journal of Petrology, 57(6): 1135-1170.

Cooper, G.F., Wilson, C.J., Millet, M.-A., Baker, J.A., Smith, E.G., 2012. Systematic tapping of independent magma chambers during the 1Ma Kidnappers supereruption. Earth and Planetary Science Letters, 313: 23-33.

Costa, A., Smith, V.C., Macedonio, G., Matthews, N.E., 2014. The magnitude and impact of the Youngest Toba Tuff super-eruption. Frontiers in Earth Science, 2: 16.

Dehn, J., Farrell, J.W., Schmincke, H.-U., 1991. Neogene tephrochronology from Site 758 on northern Ninetyeast Ridge: Indonesian arc volcanism of the past 5 Ma. In: Weissel, J., Peirce, J., Taylor, E., Alt, J., et al. (Eds.), Proceedings Ocean Drilling Program, Scientific Results. Ocean Drilling Programme, College Station, Texas, pp. 273-295.

Gardner, J.E., Layer, P.W., Rutherford, M.J., 2002. Phenocrysts versus xenocrysts in the youngest Toba Tuff: Implications for the petrogenesis of 2800 km3 of magma. Geology, 30(4): 347-350.

Gatti, E., 2012. Geochemical and sedimentological investigations of Youngest Toba Tuff ashfall deposits., Unpublished PhD Thesis, University of Cambridge.

Gatti, E., Durant, A.J., Gibbard, P.L., Oppenheimer, C., 2011. Youngest Toba Tuff in the Son Valley, India: a weak and discontinuous stratigraphic marker. Quaternary Science Reviews, 30: 3925-3934.

Gatti, E., Oppenheimer, C., 2012. The utilization of distal tephra records for understanding climatic and environmental consequences of extreme eruptions: a case study from the Youngest Toba Tuff. In: Giosan, L., et al. (Eds.), Climates, Landscapes, and Civilizations. American Geophysical Union, Washington DC, pp. 67-73.

Gatti, E., Villa, I.M., Achyuthan, H., Gibbard, P.L., Oppenheimer, C., 2014. An investigation of geochemical variability in distal and proximal glass from the Youngest Toba Tuff eruption. Bulletin of Volcanology, 76(9): in press.

GeoReM, 2014. http://georem.mpch-mainz.gwdg.de/sample_query.asp.

Gravley, D., Wilson, C., Leonard, G., Cole, J., 2007. Double trouble: Paired ignimbrite eruptions and collateral subsidence in the Taupo Volcanic Zone, New Zealand. Geological Society of America Bulletin, 119(1-2): 18-30.

Gualda, G.A., Ghiorso, M.S., 2013a. The Bishop Tuff giant magma body: an alternative to the Standard Model. Contributions to Mineralogy and Petrology, 166(3): 755-775.

Gualda, G.A., Gravley, D.M., Deering, C.D., Ghiorso, M.S., 2019. Magma extraction pressures and the architecture of volcanic plumbing systems. Earth and Planetary Science Letters, 522: 118-124.

Gualda, G.A.R., Ghiorso, M.S., 2013b. Low-pressure origin of high-silica rhyolites and granites. Journal of Geology, 121(5): 537-545.

Gualda, G.A.R., Ghiorso, M.S., 2014. Phase-equilibrium geobarometers for silicic rocks based on rhyolite-MELTS. Part 1: Principles, procedures, and evaluation of the method. Contributions to Mineralogy and Petrology, 168(1): 1033.

Gualda, G.A.R., Ghiorso, M.S., Lemons, R.V., Carley, T.L., 2012. Rhyolite-MELTS: a modified calibration of MELTS optimized for silica-rich, fluid-bearing magmatic systems. Journal of Petrology, 53(5): 875-890.

Hamilton, D.L., MacKenzie, W.S., 1965. Phase equilibrium studies in the system $NaAlSi0_4$ (nepheline)-$KAlSi0_4$ (kalsilite) - $Si0_2$ - H_20. Mineralogical Magazine, 34: 214-231.

Jaxybulatov, K., Shapiro, N., Koulakov, I., Mordret, A., Landès, M., Sens-Schönfelder, C., 2014. A large magmatic sill complex beneath the Toba caldera. science, 346(6209): 617-619.

Jochum, K.-P., Stoll, B., 2008. Reference materials for elemental and isotopic analysis by LA-(MC)-ICP-MS: Successes and outstanding needs. In: Sylvester, P. (Ed.), Laser Ablation-ICP-MS in the Earth Sciences, Current practices and outstanding issues. Mineralogical Association of Canada (MAC) Short Course Series, Vancouver, pp. 147-168.

Jochum, K.P., Stoll, B., Herwig, K., others, 2006. MPI-DING reference glasses for in situ microanalysis: New reference values for element concentrations and isotope ratios. Geochemistry, Geophysics, Geosystems, 7: Q02008, doi:10.1029/2005GC001060.

Kennedy, B., Holohan, E., Stix, J., Gravley, D., Davidson, J., Cole, J., 2018a. Magma plumbing beneath collapse caldera volcanic systems. Earth-science reviews, 177: 404-424.

Kennedy, B.M., Holohan, E.P., Stix, J., Gravley, D.M., Davidson, J.R., Cole, J.W., Burchardt, S., 2018b. Volcanic and Igneous Plumbing Systems of Caldera Volcanoes. In: Burchardt, S. (Ed.), Volcanic and Igneous Plumbing Systems. Elsevier, pp. 259-284.

Knight, M.D., Walker, G.P., Ellwood, B.B., Diehl, J.F., 1986. Stratigraphy, paleomagnetism, and magnetic fabric of the Toba Tuffs: constraints on the sources and eruptive styles. Journal of Geophysical Research: Solid Earth, 91(B10): 10355-10382.

Koulakov, I., Kasatkina, E., Shapiro, N.M., Jaupart, C., Vasilevsky, A., El Khrepy, S., Al-Arifi, N., Smirnov, S., 2016. The feeder system of the Toba supervolcano from the slab to the shallow reservoir. Nature communications, 7: 12228.

Koulakov, I., Yudistira, T., Luehr, B.-G., 2009. P, S velocity and VP/VS ratio beneath the Toba caldera complex (Northern Sumatra) from local earthquake tomography. Geophysical Journal International, 177(3): 1121-1139.

Kuehn, S.C., Froese, D.G., Shane, P.A., 2011. The INTAV intercomparison of electron-beam microanalysis of glass by tephrochronology laboratories, results and recommendations. Quaternary International, 246: 19-47.

Lane, C.S., Chorn, B.T., Johnson, T.C., 2013. Ash from the Toba supereruption in Lake Malawi shows no volcanic winter in East Africa at 75 ka. Proceedings of the National Academy of Sciences, 110: 8025-8029.

Lee, M.-Y., Chen, C.-H., Wei, K.-Y., Y., I., Carey, S.N., 2004. First Toba supereruption revival. Geology, 32: 61-64.

Luth, W.C., Jahns, R.H., Tuttle, O.F., 1964. The granite system at pressures of 4 to 10 kilobars. Journal of Geophysical Research, 69(4): 759-773.

Mark, D.F., Petraglia, M., Smith, V.C., Morgan, L.E., Barfod, D.N., Ellis, B.S., Pearce, N.J., Pal, J., Korisettar, R., 2013a. A high-precision $^{40}Ar/^{39}Ar$ age for the Young Toba Tuff and dating of ultra-distal tephra: Forcing of Quaternary climate and implications for hominin occupation of India. Quat Geochronol, 10.

Mark, D.F., Petraglia, M.D., Smith, V.C., Morgan, L.E., Barfod, D.N., Ellis, B.S., Pearce, N.J.G., Pal, J.N., Korisettar, R., 2013b. Multiple interpretive errors? Indeed. Reply to: Climate effects of the 74 ka Toba super-eruption: multiple interpretive errors in 'A high-precision $^{40}Ar/^{39}Ar$ age for the Young Toba Tuff and dating of ultra-distal tephra' by Michael Haslam. Quaternary Geochronology, 18: 173-175.

Mark, D.F., Petraglia, M.D., Smith , V.C., Morgan, L.E., Barfod, D.N., Ellis, B.S., Pearce, N.J.G., Pal, J.N., Korisettar, R., 2014. A high-precision $^{40}Ar/^{39}Ar$ age for the Young Toba Tuff and dating of ultra-distal tephra: Forcing of Quaternary climate and implications for hominin occupation of India. Quaternary Geochronology, 21: 90-103.

Mark, D.F., Renne, P.R., Dymock, R.C., Smith, V.C., Simon, J.I., Morgan, L.E., Staff, R.A., Ellis, B.S., Pearce, N.J., 2017. High-precision 40Ar/39Ar dating of Pleistocene tuffs and temporal anchoring of the Matuyama-Brunhes boundary. Quaternary Geochronology, 39: 1-23.

Masturyono, McCaffrey, R., Wark, D.A., Roecker, S.W., Fauzi, Ibrahim, G., Sukhyar, 2001. Distribution of magma beneath the Toba caldera complex, north Sumatra, Indonesia, constrained by three-dimensional P wave velocities, seismicity, and gravity data. Geochemistry, Geophysics, Geosystems, 2: 1-24.

Matthews, N.E., Smith, V.C., Costa, A., Durant, A.J., Pyle, D.M., Pearce, N.J.G., 2012. Ultra-distal tephra deposits from super-eruptions: examples from Toba and New Zealand. Quaternary International, 258: 54-79.

Mucek, A.E., Danišík, M., de Silva, S.L., Schmitt, A.K., Pratomo, I., Coble, M.A., 2017. Post-supereruption recovery at Toba Caldera. Nature communications, 8: 15248.

Neudorf, C.M., Roberts, R.G., Jacobs, Z., 2014. Assesing the time of final deposition of the Youngest Toba Tuff depsoits in the Middle Son Valley, northern India. Palaeogeography, Palaeoclimatology, Palaeoecology, 399: 127-139.

Ninkovich, D., Shackleton, N.J., Abdel-Monem, A.A., Obradovich, J.D., Izett, G.A., 1978. K-Ar age of the late Pleistocene eruption of Toba, north Sumatra. Nature 276: 574-577.

Oppenheimer, C., 2002. Limited global change due to the largest known Quaternary eruption, Toba≈ 74 kyr BP? Quaternary Science Reviews, 21(14-15): 1593-1609.

Oppenheimer, C., 2011. Eruptions that shook the world. Cambridge University Press, 392 pp.

Pamukcu, A.S., Gualda, G.A., Bégué, F., Gravley, D.M., 2015. Melt inclusion shapes: Timekeepers of short-lived giant magma bodies. Geology, 43(11): 947-950.

Pattan, J.N., Pearce, N.J.G., Banakar, V.K., Parthiban, G., 2002. Origin of ash i the Central Indian Ocean Basin and its implication for the volume estimate of the 74,000 year BP Youngest Toba eruption. Current Science: 889-893.

Pattan, J.N., Prasad, M.S., Babu, E.V.S.S.K., 2010. Correlation of the oldest Toba Tuff to sediments in the central Indian Ocean Basin. Journal of Earth System Science, 119: 531-539.

Pattan, J.N., Shane, P.A.R., Banakar, V.K., 1999. New occurrence of Youngest Toba Tuff in abyssal sediments of the Central Indian Ocean Basin. Marine Geology, 155: 243-248.

Pattan, J.N., Shane, P.A.R., Pearce, N.J.G., Banakar, V.K., Parthiban, G., 2001. An occurrence of the ~74 ka Youngest Toba Tephra from the Western continental margin of India. Current Science, 80: 1322-1326.

Pearce, N.J.G., 2014. Towards a protocol for the trace element analyses of glass from rhyolitic shards in tephra deposits by laser ablation ICP-MS. Journal of Quaternary Science, 29: 627-640.

Pearce, N.J.G., Denton, J.S., Perkins, W.T., Westgate, J.A., Alloway, B.V., 2007. Correlation and characterisation of individual glass shards from tephra deposits using trace element laser ablation ICP-MS analyses: current status and future potential. Journal of Quaternary Science, 22: 721-236.

Pearce, N.J.G., Perkins, W.T., Westgate, J.A., Gorton, M.P., Jackson, S.E., Neal, C.R., Chenery, S.P., 1997. A compilation of new and published major and trace element data for NIST SRM 610 and NIST SRM 612 glass reference materials. Geostandards Newsletter, 21: 115-144.

Pearce, N.J.G., Perkins, W.T., Westgate, J.A., Wade, S.C., 2011. Trace element analysis by laser ablation ICP-MS: the quest for comprehensive chemical characterisation of single sub-10um volcanic glass shards. Quaternary International, 246: 57-81.

Pearce, N.J.G., Westgate, J.A., Gatti, E., Pattan, J.N., Parthiban, G., Achyuthan, H., 2014. Individual glass shard trace element analyses confirm that all known Toba tephra reported from India is from the 75 ka Youngest Toba eruption. Journal of Quaternary Science, 29: 729-734.

Pearce, N.J.G., Westgate, J.A., Perkins, W.T., Preece, S.J., 2004. The application of ICP-MS methods to tephrochronological problems. Applied Geochemistry, 19: 289-322.

Petraglia, M.D., Korisettar, R., Pal, J.N., 2012. The Toba volcanic super-eruption of 74,000 years ago: climate change, environments, and evolving humans. Quaternary International, 258: 1-4.

Rampino, M., Ambrose, S.H., 2000. Volcanic winter in the Garden of Eden: the Toba supereruption and the late Pleistocene human population crash. In: McCoy, F.W., Heiken, G. (Eds.), Volcanic hazards and disasters in human antiquity. Geological Society of America, Boulder, Colorado, pp. 71-82.

Reid, M.R., Vazquez, J.A., 2017. Fitful and protracted magma assembly leading to a giant eruption, Youngest Toba Tuff, Indonesia. Geochemistry, Geophysics, Geosystems, 18(1): 156-177.

Roberts, R.G., Storey, M., Haslam, M., 2013. Toba supereruption: Age and impact on East African ecosystems. Proceedings of the National Academy of Sciences, 110(33): E3047-E3047.

Rose, W.I., Chesner, C.A., 1987. Dispersal of ash in the great Toba eruption, 75 ka. Geology, 15(10): 913-917.

Schott, F.A., McCreary Jr, J.P., 2001. The monsoon circulation of the Indian Ocean. Progress in Oceanography, 51(1): 1-123.

Schulz, H., von Rad, U., Erlenkeuser, H., 1998. Correlation between Arabian Sea and Greenland climate oscillations of the past 110,000 years. Nature, 393(6680): 54.

Shane, P.A.R., Westgate, J.A., Williams, M.A.J., Korisettar, R., 1995. New geochemical evidence for the Youngest Toba Tuff in India. Quaternary Research, 44: 200-204.

Smith, E.I., Jacobs, Z., Johnsen, R., Ren, M., Fisher, E.C., Oestmo, S., Wilkins, J., Harris, J.A., Karkanas, P., Fitch, S., Ciravolo, A., Keenan, D., Cleghorn, N., Lane, C.S., Mattthews, T., Marean, C.W., 2018. Humans thrived in South Africa through the Toba eruption about 74,000 years ago. Nature, 555(7697): 511.

Smith, V.C., Pearce, N.J.G., Matthews, N.E., Westgate, J.A., Petraglia, M.D., Haslam, M., Lane, C.S., Korisettar, R., Pal, J.N., 2011. Geochemical fingerprinting the widespread Toba tephra using biotite compositions. Quaternary International, 246: 97-104.

Storey, M., Roberts, R.G., Saidin, M., 2012. Astronomically calibrated $^{40}Ar/^{39}Ar$ age for the Toba supereruption and global synchronization of late Quaternary records. Proceedings of the National Academy of Sciences, 109(46): 18684-18688.

Sun, S.-s., McDonough, W.F., 1989. Chemical and isotopic systematics of oceanic basalts: implications for mantle compositions and processes. In: Saunders, A.D., Norry, M.J. (Eds.), Magmatism in the Ocean Basins. Geological Society Special Publication, pp. 313-345.

Swallow, E.J., Wilson, C.J., Myers, M.L., Wallace, P.J., Collins, K.S., Smith, E.G., 2018. Evacuation of multiple magma bodies and the onset of caldera collapse in a supereruption, captured in glass and mineral compositions. Contributions to Mineralogy and Petrology, 173(4): 33.

Tramontano, S., Gualda, G.A., Ghiorso, M.S., 2017. Internal triggering of volcanic eruptions: tracking overpressure regimes for giant magma bodies. Earth and Planetary Science Letters, 472: 142-151.

Tuttle, O.F., Bowen, N.L., 1958. Origin of granite in the light of experimental studies in the system $NaAlSi_3O_8$ - $KAlSi_3O_8$ - SiO_2 - H_2O. Geological Society of America Memoir 74, 146 pp.

Wallace, P.J., Anderson Jr, A.T., Davis, A.M., 1999. Gradients in H2O, CO2, and exsolved gas in a large-volume silicic magma system: Interpreting the record preserved in melt inclusions from the Bishop Tuff. Journal of Geophysical Research: Solid Earth, 104(B9): 20097-20122.

Watson, E.B., Harrison, T.M., 1983. Zircon saturation revisited: temperature and composition effects in a variety of crustal magma types. Earth and Planetary Science Letters, 64(2): 295-304.

Weber, M., Wiedicke-Hombach, M., Kudrass, H., Erlenkeuser, H., 2003. Bengal Fan sediment transport activity and response to climate forcing inferred from sediment physical properties. Sedimentary Geology, 155(3): 361-381.

Westaway, R., Mishra, S., Deo, S., Bridgland, D.R., 2011. Methods for determination of the age of Pleistocene tephra, derived from eruption of Toba, in central India. Journal of Earth System Science, 120: 503-530.

Westgate, J.A., Pearce, N.J.G., 2017. Quaternary tephrochronology of the Toba tuffs and its significance with respect to archaeological studies in peninsular India. In: Prehistory to Early History. In: Korisettar, R. (Ed.), Beyond Stones and More Stones - Issues in Indian Archaeology:. The Mythic Society, Bengaluru, India, pp. 199-233.

Westgate, J.A., Pearce, N.J.G., Gatti, E., Achyuthan, H., 2014. Distinction between the Youngest Toba Tuff and Oldest Toba Tuff from northern Sumatra based on the area density of spontaneous fission tracks in their glass shards. Quaternary Research, 82: 388-393.

Westgate, J.A., Pearce, N.J.G., Perkins, W.T., Preece, S.J., Chesner, C.A., Muhammad, R.F., 2013. Tephrochronology of the Toba tuffs: four primary glass populations define the 75 ka Youngest Toba Tuff, northern Sumatra, Indonesia. Journal of Quaternary Science, 28: 772-776.

Westgate, J.A., Shane, P.A., Pearce, N.J.G., Perkins, W.T., Korisettar, R., Chesner, C.A., Williams, M.A.J., Acharyya, S.K., 1998. All Toba tephra occurrences across peninsular India belong to the 75,000 yr B.P. eruption. Quaternary Research, 50: 107-112.

Westgate, J.A., WoldeGabriel, G., Halls, H.C., Bray, C.J., Barendregt, R.W., Pearce, N.J.G., Sarna-Wojcicki, A.M., Gorton, M.P., Kelley, R.E., Schultz-Fellenz, E., 2019. Quaternary tephra from

Valles caldera in the volcanic field of New Mexico, identified in western Canada. Quaternary Research, 91: 813-828.
Williams, M.A.J., 2012. The ~73ka Toba super-eruption and its impact: History of a debate. Quaternary International, 258: 19-29.
Wolff, J.A., Ellis, B., Ramos, F.C., Starkel, W.A., Boroughs, S., Olin, P.H., Bachmann, O., 2015. Remelting of cumulates as a process for producing chemical zoning in silicic tuffs: A comparison of cool, wet and hot, dry rhyolitic magma systems. Lithos, 236: 275-286.
Woods, A.W., Wohletz, K., 1991. Dimensions and dynamics of co-ignimbrite eruption columns. Nature, 350(6315): 225.